5 BASIC CONCEPTS IN DATA PROCESSING

Lead Authors: Viktor Feygels[a] and Yuri Kopilevich[b]

Contributing Authors: Minsu Kim[c], Chi-Kuei-Wang[d]

a) Teledyne Optech Inc., 7225 Stennis Airport Drive, Suite 400, Kiln, MS 39556
b) St. Petersburg State University of Information Technologies, Mechanics and Optics
c) USGS, 47914 252Nd Street, Sioux Falls, SD
d) Department of Geomatics, National Cheng Kung Univ., Tainan, Taiwan

5.1 Direct georeferencing of the lidar point

Minsu Kim

Lidar data processing is usually considered to be synonymous with the production of a digital elevation model (DEM). While this is obviously critical – and the topic of this section – some advanced ALB systems are radiometrically calibrated so that the data can also be used to estimate the optical properties of a water body and the reflectance of the ocean bottom, topics which will be treated in Sections 5.2, 5.3 and 5.4. Still, the heart of the lidar system is to produce a georeferenced point cloud of laser bathymetry measurements. This introductory section is devoted to describing the georeferencing of the lidar point cloud. All modern airborne lidar imaging systems use direct georeferencing, using an IMU (inertial measurement unit) together with the GNSS (global navigation satellite system) in order to obtain position and orientation. The georeferencing of each lidar point then requires a sequence of coordinate transformations and translations between a series of reference frames.

5.1.1 Sensor modeling

Airborne lidar systems use scanning devices to distribute observations on a surface, making the lidar an imaging system. There are several different types of scanning mechanisms, each of which distributes laser measurements in a different pattern. Examples (with the associated scanning patterns) are: oscillating mirror (zigzag), rotating polygon mirror (parallel lines), nutating mirror (overlapping ellipse), and rotating prism (overlapping circle).

The first step in defining a mathematical model of a scanning system (scanner model) is to define a proper 3D Cartesian coordinate system to describe the direction vector of the laser pulse propagation. This Cartesian reference coordinate system is defined based on the sensor body, and thus is called a sensor body frame (SBF). The simplest example of an SBF would be the case of a bidirectional oscillating scanning mirror. Figure 5.1.1 illustrates the scan pattern and the definition of the sensor model. Usually the sensor is installed on the aircraft so that x-axis and y-axis are aligned to the nose (forward) and the right wing (starboard) of the aircraft, respectively. Then, according to the right-hand rule, the z-axis points downward.

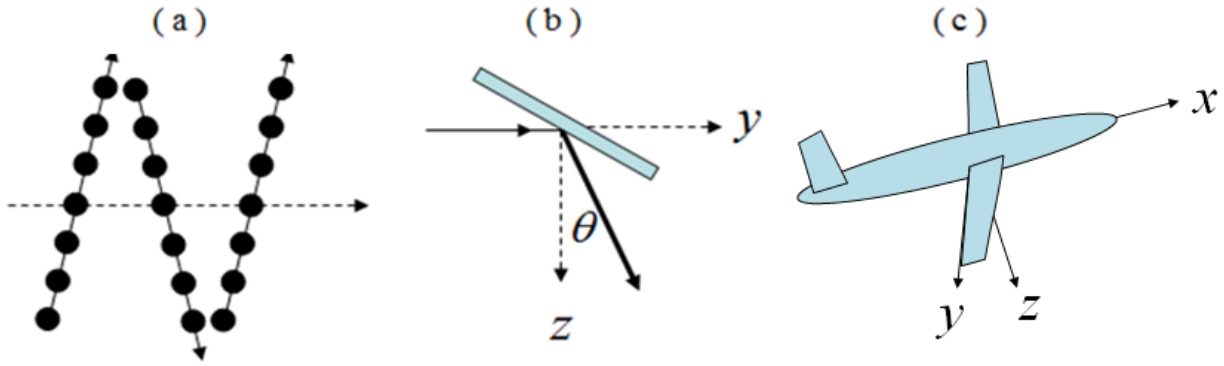

Figure 5.1.1 (a) scan pattern of the oscillating mirror scanner (b) laser pulse direction with scan angle θ_a in SBF (b) typical installation of the sensor with SBF extended on the aircraft

The sensor model in this case is simply a function of the scan angle, θ. The normalized direction vector directed toward the surface point O_w in the SBF is defined as:

$$\mathbf{d}_{O_w}^{SBF} = [0, \sin\theta, \cos\theta]^T \quad . \tag{5.1.1}$$

This direction vector is valid only for a simple oscillating mirror. The exact direction vector depends on the sensor model for the specific scanning device. Describing the details for different types of scanning systems is beyond the scope of this document, but it is important to note that the determination of the precise scan angle, θ, for each laser pulse is not a simple matter. Each scanner is equipped with an encoder that records the GNSS-synchronized time for the moment of encoding. For instance, if a system has a 30 Hz scanner rate, it records 30 GNSS times. However, the precise direction of the laser pulse propagation at the time of encoding is not known. As a result, the precise angular offset at the time of encoding is very difficult to measure. In addition, while the IMU system is installed so that its coordinates align as closely as possible to those of the optical sensor, there is always a small misalignment that must be accounted for (boresight procedure). It is also very difficult to make direct measurements of these three angles. Thus, in all lidar scanning system the boresight procedure (i.e., calculation of the angular offsets between the ALB system and the aircraft) includes this scanner offset angle as well as the usual three angular misalignment angles that are determined via optimization during calibration.

5.1.2 The position vector in the IBF

The range, r_a, that the lidar system measures is from the SBF origin (O_SBF) to the surface that reflects the laser pulse. The position vector in the SBF is determined by:

$$\boldsymbol{X}_{O_w}^{SBF} = r_a \cdot \mathbf{d}_{O_w}^{SBF} \quad . \tag{5.1.2}$$

The 3-element position vector, $\boldsymbol{X}_{O_w}^{SBF}$, represents the SBF Cartesian coordinates of the lidar point, O_w, from which the earth surface reflects the laser pulse back to the receiver. Coordinates expressed in SBF, however, are not useful by themselves (i.e., in the ALB reference system) because the reference system is not geo-referenced to a known datum. The position vector in SBF must be converted to the position vector in a global geodetic frame in a sequence of coordinate transformations.

In order to convert a position vector in an arbitrary SBF into the position vector in a global geodetic frame, the information contained in the GNSS antenna position and the IMU orientation is used to establish an IMU body frame (IBF). The IBF is a 3D Cartesian frame whose origin (O_IBF) is at the IMU center, and the definition of the coordinate system is usually printed on the top surface of the IMU housing. The physical location of the lidar point is invariant, but the coordinate representation can change depending on which reference coordinate system is used. Thus, the position vector in SBF, $\boldsymbol{X}_{O_w}^{SBF}$, is transformed to the position vector in IBF using the following relationship:

$$\boldsymbol{X}_{O_w}^{IBF} = \boldsymbol{R}_{SBF}^{IBF} \cdot \boldsymbol{X}_{O_w}^{SBF} + \boldsymbol{X}_{O_{SBF}}^{IBF} \quad , \tag{5.1.3}$$

where, $\boldsymbol{X}_{O\_SBF}^{IBF}$ is the lever-arm vector to the SBF origin in the IBF, and $\boldsymbol{R}_{SBF}^{IBF}$ is a rotation matrix that transforms $\boldsymbol{X}_{O_w}^{SBF}$ to $\boldsymbol{X}_{O_w}^{IBF}$ is defined using three boresighting angles that represent roll (ω), pitch (φ), and yaw ((κ)):

$$\boldsymbol{R}_{SBF}^{IBF} = \begin{bmatrix} \cos\kappa & -\sin\kappa & 0 \\ \sin\kappa & \cos\kappa & 0 \\ 0 & 0 & 1 \end{bmatrix} \begin{bmatrix} \cos\varphi & 0 & \sin\varphi \\ 0 & 1 & 0 \\ -\sin\varphi & 0 & \cos\varphi \end{bmatrix} \begin{bmatrix} 1 & 0 & 0 \\ 0 & \cos\omega & -\sin\omega \\ 0 & \sin\omega & \cos\omega \end{bmatrix} \tag{5.1.4}$$

$$= \begin{bmatrix} \cos\varphi\cos\kappa & \sin\omega\sin\varphi\cos\kappa - \cos\omega\sin\kappa & \cos\omega\sin\varphi\cos\kappa + \sin\omega\sin\kappa \\ \cos\varphi\sin\kappa & \sin\omega\sin\varphi\sin\kappa + \cos\omega\cos\kappa & \cos\omega\sin\varphi\sin\kappa - \sin\omega\cos\kappa \\ -\sin\varphi & \sin\omega\cos\varphi & \cos\omega\cos\varphi \end{bmatrix}$$

5.1.3 The position vector in the Local Geodetic Frame (LGF)

The success of direct georeferencing depends on the accuracy with which the position and the orientation parameters are measured using the IMU-GNSS subsystem. Once the position vector in the IBF reference system, $\boldsymbol{X}_{O_w}^{IBF}$, is known, it is transformed into a new position vector in a local geodetic frame (LGF), $\boldsymbol{X}_P^{LGF}$. An LGF is defined in reference to a global geodetic frame, such as WGS84. An arbitrary position on a local tangent plane is defined with a positive x-axis pointing to the local north (N), a positive y-axis pointing to the local east (E), and a positive z-axis pointing downward (D) to the center of the ellipsoid. Thus, the arbitrary position follows a coordinate axes convention of a North-East-Down (NED) reference frame. The orientation of the IBF with respect to the LGF is described by three angles: roll (R), pitch (P), and heading (H):

$$\boldsymbol{R}_{IBF}^{LGF} = \begin{bmatrix} \cos H & -\sin H & 0 \\ \sin H & \cos H & 0 \\ 0 & 0 & 1 \end{bmatrix} \begin{bmatrix} \cos P & 0 & \sin P \\ 0 & 1 & 0 \\ -\sin P & 0 & \cos P \end{bmatrix} \begin{bmatrix} 1 & 0 & 0 \\ 0 & \cos R & -\sin R \\ 0 & \sin R & \cos R \end{bmatrix} \tag{5.1.5}$$

$$= \begin{bmatrix} \cos P\cos H & \sin R\sin P\cos H - \cos R\sin H & \cos R\sin P\cos H + \sin R\sin H \\ \cos P\sin H & \sin R\sin P\sin H + \cos R\cos H & \cos R\sin P\sin H - \sin R\cos H \\ -\sin P & \sin R\ \cos P & \cos R\cos P \end{bmatrix}$$

Thus, the position vector $\boldsymbol{X}_{O_w}^{IBF}$ is transformed to the position vector in the LGF as follows

$$\boldsymbol{X}_{O_w}^{LGF} = \boldsymbol{R}_{IBF}^{LGF} \cdot \boldsymbol{X}_{O_w}^{IBF} \quad . \tag{5.1.6}$$

Note that there is no lever-arm vector correction because the origin of LGF is identical to O_IBF.

5.1.4 Refraction into the water

In case of ALB system only a small fraction of the laser pulse energy is reflected at the air-water interface to produce a surface return in the lidar waveform (Chapter 0). The majority of the energy is refracted into the water and propagates until it reaches the bottom where it is reflected back up to the system, producing a bottom return in the waveform. The two returns, one from the surface and one from the bottom, define the slant range in the water. By taking the refracted direction and the in-water range into account it is possible to calculate the 3D digital elevation model (DEM) of the ocean floor.

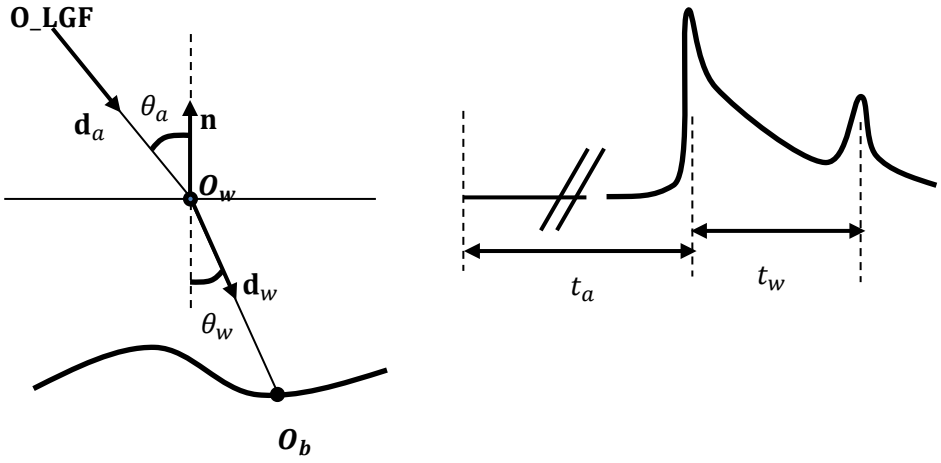

Figure 5.1.2 Refraction at the air-water interface and the waveform

It is important to note that it is only possible to calculate the refraction after the position vector is represented in LGF. This is because the x,y-plane of the SBF and IBF are not parallel to the water surface. There is also a slight mismatch between the local ellipsoid surface and the water surface; this inaccuracy is minimal for the purpose of in-water ranging.

The position vector, $X_{O_w}^{LGF}$, is the vector from O_LGF to the surface point O_w in Figure 5.1.2. The time of travel, t_a, from origin to the first peak of the waveform is related to the in-air range H_s by the relationship, $H_s = c \cdot t_a/2$. Using the vector version of Snell's law, the air-incident angle is calculated as:

$$\cos\theta_a = -\mathbf{n} \cdot \mathbf{d}_{O_w}^{LGF} \quad , \qquad \mathbf{d}_a = \boldsymbol{X}_{O_w}^{LGF}/H_s \quad . \tag{5.1.7}$$

Here, $\mathbf{d}_a$ is a unit in-air direction vector and $\mathbf{n}$ is an upward normal vector at the water surface. If we write $\boldsymbol{X}_{O_w}^{LGF} = [x, y, z]$ with $\mathbf{n} = [0, 0, -1]$, then equation (5.1.7) reduces to: $\cos\theta_a = z/H_s$.
Subsequently, the in-water refracted angle is calculated using the refractive index of water, n_w, such that

$$\cos\theta_w = \sqrt{1 - \sin^2\theta_a / n_w^2} \quad , \qquad \sin^2\theta_a = -(z/H_s)^2 \quad . \tag{5.1.8}$$

The unit direction vector of the in-water refracted beam is calculated as:

$$\mathbf{d}_{P_b}^{LGF} = (1/n_w) \cdot \mathbf{d}_a + [(1/n_w)\cos\theta_a - \cos\theta_w] \cdot \mathbf{n}. \tag{5.1.9}$$

Finally, the position vector at the ocean bottom point, O_b, is described by:

$$\mathbf{X}_{P_b}^{LGF} = \mathbf{X}_{O_w}^{LGF} + r_w \cdot \mathbf{d}_w \ , \quad h_s = c \cdot t_w/(2n_w) \quad , \tag{5.1.10}$$

where t_w is the travel time in water. If the lidar point is at the ocean bottom, $\mathbf{X}_{P_b}^{LGF}$ can be used in the place of $\mathbf{X}_{O_w}^{LGF}$ in the subsequent georeferencing calculations.

5.1.5 The position vector in the earth centered, earth fixed (ECEF) frame

The position of the phase center of the GNSS antenna can be provided by either in an ECEF (earth centered earth fixed) frame (using Cartesian coordinates or geographic coordinates) or in global ellipsoid datum (using geographic coordinates). Once the position of the GNSS antenna phase center is known, then the lever-arm distances between the IMU origin and the antenna can be used to calculate the position of the O_IBF (which is same as O_LGF). Using the latitude ϕ, longitude λ, and ellipsoid height, h, from O_LGF, it is possible to form a rotation matrix that transforms an arbitrary position vector in LGF to the position vector in ECEF:

$$\begin{aligned}
&\boldsymbol{R}_{LGF}^{ECEF} \\
&= \begin{bmatrix} \cos\lambda & -\sin\lambda & 0 \\ \sin\lambda & \cos\lambda & 0 \\ 0 & 0 & 1 \end{bmatrix} \begin{bmatrix} \cos\left(-\varphi - \frac{\pi}{2}\right) & 0 & \sin\left(-\varphi - \frac{\pi}{2}\right) \\ 0 & 1 & 0 \\ -\sin\left(-\varphi - \frac{\pi}{2}\right) & 0 & \cos\left(-\varphi - \frac{\pi}{2}\right) \end{bmatrix} \begin{bmatrix} 1 & 0 & 0 \\ 0 & \cos 0 & -\sin 0 \\ 0 & \sin 0 & \cos 0 \end{bmatrix} \\
&= \begin{bmatrix} -\sin\varphi\cos\lambda & -\sin\lambda & -\cos\varphi\cos\lambda \\ -\sin\varphi\sin\lambda & \cos\lambda & -\cos\varphi\sin\lambda \\ \cos\varphi & 0 & -\sin\varphi \end{bmatrix}
\end{aligned} \tag{5.1.11}$$

In addition to the rotation matrix, the geodetic position (φ, λ, h) of O_LGF itself can be transformed into the position in the ECEF coordinate using the following relationship:

$$\boldsymbol{R}_{O\_LGF}^{ECEF} = \begin{bmatrix} (r_N + h)\cos\varphi\cos\lambda \\ (r_N + h)\cos\varphi\sin\lambda \\ [(1 - e^2)r_N + h]\sin\varphi \end{bmatrix} \quad , \quad r_N = \frac{a}{\sqrt{1 - e^2\sin^2\varphi}} \quad , \tag{5.1.12}$$

where, a is the semi-major axis, e is the eccentricity, and r_N is the position in ECEF coordinates. We may now solve for the position vector in ECEF coordinates:

$$\boldsymbol{X}_{O_w}^{ECEF} = \boldsymbol{R}_{LGF}^{ECEF} \cdot \boldsymbol{X}_{O_w}^{LGF} + \boldsymbol{X}_{O\_LGF}^{ECEF} \tag{5.1.13}$$

The goal of georeferencing is achieved by calculating the position of the lidar point in ECEF. In practice, however, the ECEF reference system is not a convenient form for geospatial data. Most mapping products are in ellipsoidal reference systems (latitude/longitude/ellipsoid height). Thus, there is a need to convert the laser measurements from an ECEF reference system to an ellipsoidal reference system. The final

product may also need to be projected to a map coordinate system (e.g., Universal Transverse Mercator or local state plane), depending on the application.

5.2 Inverse problems of lidar waveform processing

V. Feygels, Yu. Kopilevich

Retrieval of inherent optical properties (IOPs) of seawater from ALB data represents a supplemental application of bathymetrical lidar systems, along with bottom reflectance measurement. Bottom reflectance is considered later in Section 4.4. In this Section, a general approach to the inverse problem of lidar waveform processing (initially proposed in Kopilevich et al. (2005)), is discussed; the special problem of estimation of the diffuse attenuation coefficient is considered further in Section 5.3.

As was discussed above in Section 4.3.1, processing of an experimentally obtained waveform, $D^{exp}(t)$ (the output electrical signal from the receiver channel) in order to estimate environmental properties (bottom depth, reflectance, and IOPs) relies on a comparison of the experimental waveform with simulated waveforms. To perform the comparison in the optical domain using radiometric units, the electrical signal (in digital counts) must be transformed into the optical signal, S_R^{exp} in Watts ("real waveform", see Equation (4.3.12)

$$S_R^{exp}(t) = \chi^{-1}\left[D^{exp}(t)\right] \quad , \tag{5.2.1}$$

where, $\chi^{-1}[\cdot]$ is the inverse of the channel Watt-count characteristic, $\chi[\cdot]$, which is determined from radiometric calibration of the receiving channel (Section 3.3.1).

A (simulated) waveform, $S_R^{sim}(t)$, may be calculated from a theoretically derived Impulse Response Function, $S_\delta(t)$, i.e. the lidar signal corresponding to an infinitesimally short (delta-function shaped) initial laser pulse (see Section 3.2.2). Following the same procedure presented in Section 3.3.2, $S_R^{sim}(t)$ may be calculated by convolving $S_\delta(t)$ with the effective sounding pulse shape (or the channel response function), $R(t)$:

$$S_R^{sim}(t) = \int_{-\infty}^{\infty} S_\delta(t-t') \cdot R(t')dt' \equiv S_\delta(t) * R(t) \quad , \tag{5.2.2}$$

where $R(t)$, is determined from radiometric calibration measurements (see Section 3.3.1).

Water IOPs are estimated by fitting the simulated signal, $S_R^{sim}(t)$, to the actual experimental waveform, $S_R^{exp}(t)$, on a time interval, $t_- \le t \le t_+$, where t_- corresponds to a near-surface horizon deep enough to obviate the need to account for surface effects, and t_+ corresponds to a near-bottom horizon for which bottom reflection is still undetected. The problem formally reduces to minimizing the difference between the two functions using appropriate metrics. Using the least squares method, the functional of the pulse energy, Q, may be written as:

$$Q = \int_{t_-}^{t_+} \left|S_R^{\exp}(t) - S_R^{sim}(t)\right|^2 dt \quad . \tag{5.2.3}$$

In reality, one uses the discrete analogue of the functional, i.e., the sum of the squared differences between the experimental waveform samples, $\{S_R^{\exp}(t_i)\},\ t_- \le t_i \le t_+,\ i = 1,\ 2,\ \ldots$, and the corresponding discrete values $\{S_R^{sim}(t_i)\}$.

It should be recognized that the estimates obtained with the above algorithms, using simulated waveforms calculated for a homogeneous water column, ignore vertical stratification of water optical properties and thus correspond to effective (or "averaged") values of the IOPs. The estimates are also subject to any inaccuracies of the accepted models: small-angle scattering approximation for the RTE, models used for emitted laser pulse and receiver channel, modeled VSF (Kopilevich, Kononenko, and Zadorozhnaya 2011). Corresponding errors in the IOP estimates are difficult to assess.

Unfortunately, a straightforward approach to the problem of minimization of the pulse energy functional (Equation (5.2.3)) as a variational problem using the absorption coefficient, a, backscattering coefficient, b_b, forward-scattering coefficient, b_f, and VSF shape parameter m (see Sec. 4.3.3, Equation (4.3.77) is mathematically ill-posed. However, it is possible to regularize the fitting problem using statistical relationships among the IOPs in order to restrict *a priori* the range of acceptable solutions (Dolin et al. 1988). A practical realization of the approach consists of the following steps:

Step 1. The beam attenuation coefficient, *c*, is taken as an independent variable in order to obtain an estimate, c^*, which minimizes the functional (4.2.3),

$$Q(c^*) = \min_c Q(c) \quad . \tag{5.2.4}$$

All the other IOPs are calculated for a given value of c via a set of regression relations. The single-scattering albedo ω_0 (dimensionless) is evaluated as (Levin & Kopelevich, 2003) via the beam attenuation coefficient, *c*, in 1/m:

$$\omega_0 = 0.944 - 0.048/c \quad , \tag{5.2.5}$$

For the scattering coefficient, b we use the relationship:

$$b = c\omega_0 \quad . \tag{5.2.6}$$

The hydrosol (suspended particulate) volume concentration for large particles, V_{lg}, in cm^3/m^3 is then evaluated using (Dorogin, Kopelevich, Levin, & Feigels, 1988):

$$V_{lg} = 1.44 \cdot 10^{-2} + 1.68 \cdot b \quad , \tag{5.2.7}$$

where *b* is measured in m^{-1}, and

$$b = V_{sm} \cdot b_{sm} + V_{lg} \cdot b_{lg} + b_w \quad . \tag{5.2.8}$$

Here, the specific scattering coefficients for small, b_{sm}, and large, b_{lg}, hydrosol particles, and the scattering coefficient for "pure" (hydrosol-free) seawater at 500 nm, b_w, are specified in Monin (1983) as:

$$b_{sm} = 1.34\ \mathrm{m}^{-1};\ b_{lg} = 0.312\ \mathrm{m}^{-1};\ b_w = 1.7 \cdot 10^{-3}\ \mathrm{m}^{-1}. \tag{5.2.9}$$

To be precise, equations (5.2.8) and (5.2.9) are established based on 500 nm and not 532 nm (Monin, 1983), but the corresponding error is negligible for the ALB case here. Knowing V_l and V_s, it is possible to approximate the VSF, $\beta(\theta)$, as proposed by Kopelevich & Mezhericher (1983):

$$\beta(\theta) = \left(\frac{550}{\lambda}\right)^{1.7} \cdot \beta_{sm}(\theta, 550) \cdot V_{sm} + \left(\frac{550}{\lambda}\right)^{0.3} \cdot \beta_{lg}(\theta, 550) \cdot V_{lg} + \left(\frac{550}{\lambda}\right)^{4.3} \cdot \beta_w(\theta, 550)\,, \tag{5.2.10}$$

where the wavelength, $\lambda = 532\ nm$. The functions, $\beta_{sm}(\theta, 550)$ and $\beta_l(\theta, 550)$ are the VSF for water suspensions of small and large particles respectively, for unit concentrations of the suspensions; $\beta_w(\theta, 550)$ is the VSF for pure seawater. The values of these functions are tabulated in Monin (1983) for a range of scattering angles, θ.

Integration of (5.2.10) over the appropriate solid angles gives the forward and backward scattering coefficients, b_f and b_b:

$$b_f = 2\pi \int_0^{\pi/2} \beta(\theta) \cdot \sin(\theta)\, d\theta \quad , \quad b_b = 2\pi \int_{\pi/2}^{\pi} \beta(\theta) \cdot \sin(\theta)\, d\theta \quad . \tag{5.2.11}$$

Finally, the values are used to obtain the VSF asymmetry coefficient, b_f/b_b, and the average cosine of the scattering angle, $\overline{\cos\theta}$; the latter is required for the parameter, m, in Dolin's model VSF [see Dolin & Levin (1991) and Sec. 4.3.3, Equation (4.3.77]:

$$m = [0.142 - 0.132 \cdot \overline{\cos\theta}]^{-1/2} \quad . \tag{5.2.12}$$

Equation (5.2.10) also yields an estimate for the backscattering coefficient, $\beta_\pi = \beta(180°)$. Since (5.2.12) is based on *in-situ* measurements that do not cover angles greater than ~170°, the equation does not account for the angular dependence of the VSF for angles near 180°, where a pronounced "enhanced backscattering effect" can occur (Maffione and Dana 1996). For a more realistic estimate allowing for the backscattering effect, we may use

$$\beta_\pi = C \cdot \beta(180^o) \quad , \tag{5.2.13}$$

with $\beta_\pi = \beta(180°)$ calculated from (5.2.10) and $C = \{1.3\text{-}1.9\}$

Step 2: consists of finding a better estimate of ω_0^* than that given by equation (5.2.5) by varying the value of the single scattering albedo, ω_0, at the fixed $c = c^*$:

$$Q(c^*, \omega_0^*) = \min_{\omega_0} Q(c^*, \omega_0) \quad . \tag{5.2.14}$$

During this estimation, all the other IOPs (a, b_b, b_f, and m) are assumed to be unambiguously defined by ω_0 using equations (5.2.6)-(5.2.8) and (5.2.10)-(5.2.12), with $c = c^*$. This step of the fitting algorithm makes it possible to account for local peculiarities of the sea water optical properties, rather than simply using equation (5.2.5), which is a statistical average over various regions of the ocean.

It is important to emphasize that the algorithm described above is limited to waters deep enough to provide an extended time interval (t_-, t_+) for which the waveform is not subject to surface or bottom effects. In accordance with the waveform components considered in Sec. 4.2.2 [see Figure 4.2.6 – Figure 4.2.8],

$$t_- \geq t^{sf} + \frac{\Delta t^{sf}}{2} + \tau_R \quad ; \quad t_+ \leq t^{bot} - \frac{\Delta t^{bot}}{2} \quad , \tag{5.2.15}$$

where the "geometrical stretch" of the surface-reflected pulse, Δt^{sf}, given by (4.2.4), depends on the lidar sounding geometry (i.e., it increases with the sounding angle, the emitter divergence, and the receiver field-of-view angle). Similarly, the reflected bottom pulse duration, Δt^{bot}, given by equation (4.2.5), is augmented by the small-angle scattering effect, and τ_R is the effective pulse duration. An additional constraint is the requirement that the received power, $S_R^{\exp}(t_+)$, exceed the output signal noise level, acknowledging the strong attenuation of the laser beam by seawater.

5.3 Estimation of the diffuse attenuation coefficient from lidar waveform slope

V. Feygels, Yu. Kopilevich

The diffuse attenuation coefficient, K_d, is a key physical characteristic in the field of ocean optics, and is a prominent example of an apparent optical properties (AOPs) (see Section 3.3.1 and (Mobley, 1994)). To calculate K_d in terms of the inherent optical properties (IOPs), the following relation proposed by Morel & Loisel (Morel & Loisel, 1998) may be applied:

$$K_d = (\cos\theta_w^{sun})^{-1} \cdot 1.0395 \cdot a_s \quad , \tag{5.3.1}$$

where 1.0395 is a theoretical constant; θ_w^{sun}, is solar zenith angle in the water; and a_s is the effective absorption coefficient. The coefficient a_s defined in Section 4.3.2 as $a_s = a + 2b_b$ (a is the absorption coefficient and b_b is the backscattering coefficient) is to be identified with the property $a + b_b$ used by Morel & Loisel (1998) and others. The ratio K_d/a_s calculated for various solar zenith angles using equation (5.3.1), are presented in Table 5.1:

Table 5.1. K_d/a_s calculated for various solar zenith angles using equation (4.3.1)

solar zenith angle			$\cos\theta_w^{sun}$	$1/\theta_w^{sun}$	K_d/a_s
in the air, θ_a^{sun} degree	in the water, θ_w^{sun}				
	Radian	Degree			
0	0	0	1	1	1.0395
5	0.0651	3.7292	0.9979	1.0021	1.041706
10	0.13	7.4458	0.9916	1.0085	1.04834
15	0.1944	11.137	0.9812	1.0192	1.05945
20	0.2581	14.788	0.9669	1.0343	1.07511
25	0.3209	18.384	0.949	1.0538	1.095406
30	0.3824	21.909	0.9278	1.0778	1.12042
35	0.4423	25.343	0.9038	1.1065	1.150196
40	0.5003	28.665	0.8774	1.1397	1.1847
45	0.5559	31.85	0.8494	1.1773	1.223753
50	0.6085	34.867	0.8205	1.2188	1.266941
55	0.6577	37.684	0.7914	1.2636	1.313506
60	0.7027	40.262	0.7631	1.3105	1.362217

In practical calculations, accounting for "reasonable" sun zenith angles for a given site latitude, the ratio K_d/a_s may be approximated by a constant. For example, an approximate relationship derived from equation (5.3.1) and Table 5.1 [see Tuell et al. (Tuell et al., 2005)]:

$$K_d = 1.17 \cdot a_s \quad , \tag{5.3.2}$$

Estimation of the diffuse attenuation coefficient from lidar sounding data consists in retrieval of the effective absorption coefficient, a_s, from the lidar waveform, and the application of equation (4.3.1) [or its approximate form analogous to equation (5.3.2)]. Formally, the value of a_s may be estimated from the inverse problem described in Section 4.2 by fitting an experimental waveform with a simulated waveform that is calculated using a variable set of IOP values. For the specific task of estimating the diffuse attenuation coefficient, however, the general ill-posed problem may be regularized without invoking statistical relationships among the IOPs. The practical approach is based on the backscattered lidar signal model (see Sections 4.3.2 and 4.3.3) for an infinitesimally short pulse, which may be written in two equivalent forms [compare with (4.3.13)]:

$$\begin{aligned} S_\delta^{back}(t) &= Q \cdot \tau_F^2 \frac{\Sigma}{(H_s n_w + h_s)^2} \beta_\pi \frac{c}{2\mathrm{n}_w} \exp\left[-2h_s \cdot K_{sys}(h_s)\right] \\ &= Q \cdot \tau_F^2 \frac{\Sigma}{(H_s n_w + h_s)^2} \beta_\pi \frac{c}{2\mathrm{n}_w} \exp(-2h_s \cdot a_s) \cdot F_D(h_s) \end{aligned} \tag{5.3.3}$$

Here the slant depth, h_s is related to the time, t, as $h_s = h_s(t) = ct/2n_w$ (where c/n_w is the speed of light in the water); Q is the energy of the incident laser pulse (taking into account the attenuation over the

atmospheric path and the transmission of the receiver system); τ_F is the Fresnel transmission of the water–air interface; Σ is the pupil area of the lidar receiver; β_π is the backscattering coefficient of sea water; and H_s is length of beam pass in the air (slant path of the lidar beam above sea level). The so-called "system attenuation coefficient", K_{sys} may then be expressed as

$$K_{sys}(h_s) = a_s + K'_{sys}(h_s) = a_s - \ln F_D(h_s) \qquad (5.3.4)$$

The function $F_D(h_s)$ was introduced by Dolin & Savel'ev (1971) [see also Dolin & Levin (1991) to account for the effect of forward scattering on the decay of the lidar signal with water depth; $F_D(h_s) = 1$ at $h_s = 0$ and decreases with the water depth. The decay rate of the function increases with the small-angle forward-scattering coefficient $b_s = b - b_b$, and strongly depends on the lidar receiver field-of-view angle Θ_R. Figure 5.3.1 illustrates the function $F_D(h_s)$, calculated for two CZMIL receiver channels: the wide-field channel ($\Theta_R = 40\ mrad$) and the narrow-field channel ($\Theta_R = 1.9\ mrad$). The IOP values used in the calculations were: $a_s = 0.075\ m^{-1}$; $b_s = 0.2\ m^{-1}$; VSF shape parameter in Dolin's model, $m = 7$. In the case of the wide-field channel, the approximation $F_D(h_s) \approx 1$ may be used for small enough depth values, $h_s \le h_s^{max}(b_s, \Theta_R)$, with the additional condition (from (4.3.4) that $K_{sys}(h_s) \approx a_s$. According to equation (3.3.1, the backscattered signal $S_\delta^{back}(t)$ for the wide-field receiver channel over the time interval, $t \le t^{sc}(b_s, \Theta_R) \equiv 2h_s^{max}(b_s, \Theta_R)/n_w c$, (where t^{sc} is the upper limit of the backscattered signal argument that corresponds to a negligible impact of forward scattering) may be approximated with the exponential relationship:

$$S_\delta^{back}(t) \approx const \cdot exp[-2h_s \cdot a_s], \qquad t \le t^{sc}(b_s, \Theta_R) \qquad (5.3.5)$$

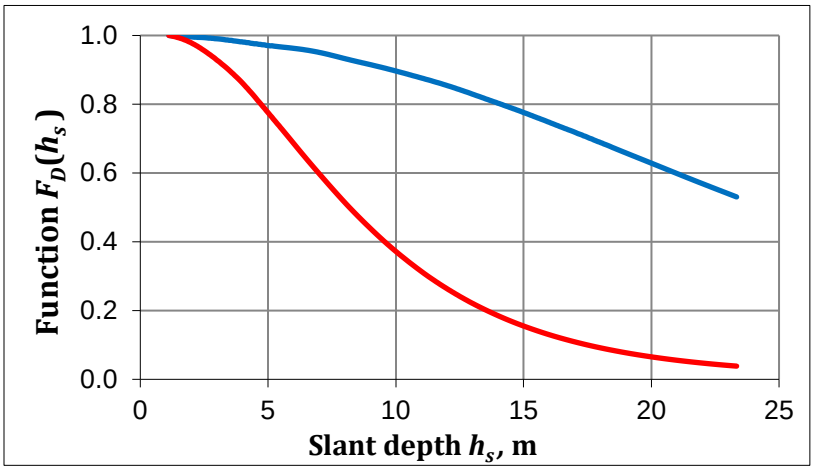

Figure 5.3.1. The function $F_D(h_s)$ calculated for the wide-field CZMIL channel with the field-of-view angle $\Theta_R = 40\ mrad$ (blue) and for the narrow-field channel with $\Theta_R = 1.9\ mrad$ (red); $a_s = 0.075\ m^{-1}$; $b_s = 0.2\ m^{-1}$; VSF shape parameter in Dolin's model $m = 7$.

Figure 4.3.2 illustrates the backscattered signal decay with slant depth. The simulated backscattered components of the waveforms $S_\delta^{back}(t)$ in each of the channels are shown as functions of the slant depth, $h_s = ct/2n_w$. It is seen that, for the narrow-field channel, the signal tends to zero at the upper limit of the time interval, $t^{sc}(b_s, \Theta_R)$, where the approximation (5.3.5) is accurate enough for realistic forward scattering.

For water that is sufficiently deep, there exists a time interval $t^{sf} + \Delta t^{sf} < t < t^{bot} - \Delta t$ (see Section 5.3.2 for the notation) for which the effects of surface and bottom reflection may be neglected. In that case, the backscattered signal $S_\delta^{back}(t)$ coincides with the ImpRF, $S_\delta(t)$ (the waveform corresponding to an infinitesimally short sounding pulse, see Section 3.3.2). In virtue of equation (4.3.5),

$$S_\delta(t) \approx const \cdot exp\left[-\frac{ct}{n}\cdot a_s\right] \quad , \quad t^{sf} + \Delta t^{sf} < t < \min\{t^{sc}(b_s, \Theta_R), t^{bot} - \Delta t^{bot}\} \quad . \qquad (5.3.6)$$

The time interval specified in equation (5.3.6) exists (is not empty) only for clear water with weak enough scattering and absorption for $S_\delta(t)$ to be well above the noise level, if the receiver field of view is wide enough to ensure existence of the time interval specified in (5.3.6).

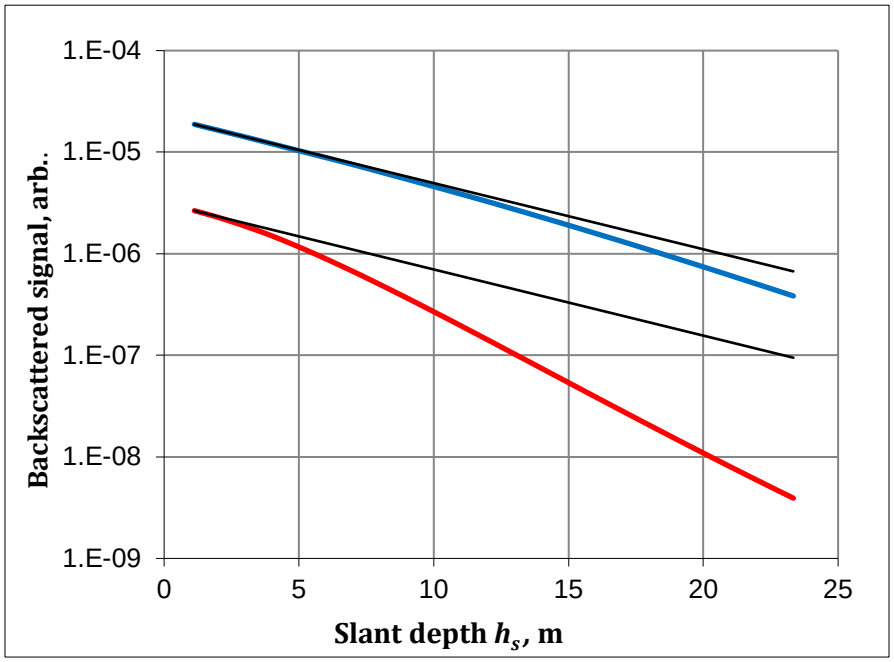

Figure 5.3.2. Backscattered components, S_δ^{back}, of delta-function sounding pulse waveforms in the wide-field CZMIL channel with the field-of-view angle, $\Theta_R = 40\ mrad$ (blue) and for the narrow-field channel with $\Theta_R = 1.9\ mrad$ (red); $a_s = 0.075\ m^{-1}$; $b_s = 0.2\ m^{-1}$; VSF shape parameter in Dolin's model $m = 7$. Black lines correspond to exponential approximation, $S_\delta^{back} \sim exp(-2a_s h_s)$.

In order to estimate the effective absorption coefficient, a_s , from the lidar waveform, it is essential that equation (4.3.6) yield a formula for the "real waveform", $S_R(t)$ [equation (4.2.8)], similar to that retrievable from the output lidar signal:

$$S_R(t) = \int_{-\infty}^{\infty} S_\delta(t - t') \cdot R(t')dt' \equiv S_\delta(t) * R(t) \quad , \qquad (5.3.7)$$

where $R(t)$ is the effective sounding pulse shape (see Section 4.3.1). In effect, equation (5.3.6) requires that:

$$\int_{-\infty}^{\infty} exp\left[-\frac{c(t-t')}{n}\cdot a_s\right]\cdot R(t')\,dt' = exp\left[-\frac{ct}{n}\cdot a_s\right]\cdot \int_{-\infty}^{\infty} exp\left[-\frac{ct'}{n}\cdot a_s\right]\cdot R(t') \qquad (5.3.8)$$

in which case (5.3.6) and (5.3.7) yield

$$S_R(t) \approx const \cdot exp\left[-\frac{ct}{n} \cdot a_s\right] \quad , \qquad t^{sf} + \Delta t^{sf} + \tau_R < t < \min\{t^{sc}(b_s, \Theta_R), t^{bot} - \Delta t^{bot}\} \quad . \tag{5.3.9}$$

Compared to equation (5.3.6), the time interval in equation (5.3.9) is reduced by the effective sounding pulse duration, τ_R.

Based on equation (5.3.9), the problem of estimating the effective absorption coefficient from the lidar waveform is reduced to the derivation of the $\{S_R(t)\}$ values from output signal samples at discrete times in the interval specified in equation (5.3.8) and a linear regression of the values in logarithmic scale ((5.3.2)). The estimate for a_s is then easily obtained from the line slope regression.

Note that the approach to estimating the diffuse attenuation coefficient from the lidar waveform calls for application of the receiver channel Watt-count characteristic (Section 4.3.1) obtained in the course of radiometric calibration of the receiver channel described in Section 4.4. Knowledge of the channel response to the laser pulse or effective pulse shape, $R(t)$, is not necessary. Applicability of the procedure described above is restricted by the limitations imposed by both environmental properties (water clarity and the sea depth) and lidar receiver characteristics (the receiver field of view, the effective sounding pulse duration). The procedure also assumes homogeneity of the water column. Thus, the estimates for the effective absorption and the diffuse attenuation coefficient obtained using this method relate to "effective averaged" values of the optical properties. It should be noted that other approaches to estimation of diffuse attenuation profiles from lidar waveforms are presented in Steinvall, Koppari, & Karlson (1993) and Smart & Kwon (1996).

5.4 Bottom reflectance estimation

Yuri Kopilevich and Chi-Kuei Wang

The ability to estimate seafloor reflectance from ALB waveforms, first demonstrated by Lee and Tuell (Lee & Tuell, 2003), may have direct value in the analysis of bottom habitat type (Tuell et al., 2005). The lidar-derived bottom reflectance is also used (together with depth) as a constraint in inversion of airborne hyperspectral imagery data for benthic mapping applications (Park et al., 2010; Tuell et al., 2005; Tuell & Park, 2004).

As indicated above in 5.1 (see also 4.3.1), processing experimentally obtained waveforms in order to estimate bottom reflectance requires a preliminary transformation from the output electrical signal from the receiver channel, $D^{exp}(t)$ (in digital counts), into the optical signal, S_R^{exp} in Watts (i.e., the "real waveform", see Section 4.3.1). The channel Watt-count characteristic, $\chi[\cdot]$, used in the procedure, should be known from radiometric calibration of the receiving channel (Section 4.3.1).

In shallow water, the bottom-reflected component of the lidar return is superimposed on the backscattering from the water column (Pe'eri & Philpot, 2007) as shown in Figure 5.4.1). In deep, clear water, the backscattered signal from near-bottom water layer can be below the noise level in which case it does not interfere with the bottom-reflected pulse (Figure 5.4.2).

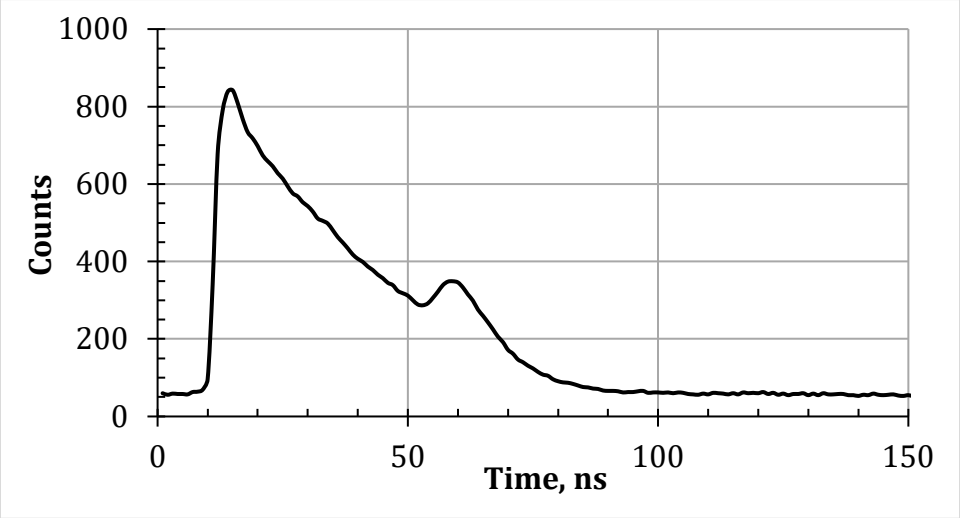

Figure 5.4.1. CZMIL waveform from the Cat Island region, Mississippi Coast; depth 6.5 m. The bottom-reflected peak rides on the background caused by backscattering from the water.

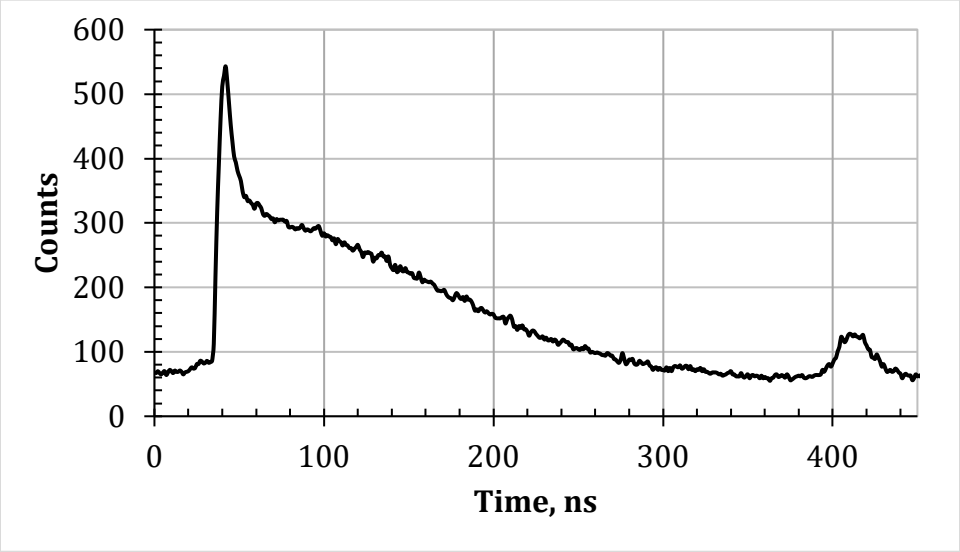

Figure 5.4.2. CZMIL waveform from the Fort Lauderdale coastal zone, Florida; depth 39 m. The backscattered signal from the near-bottom layer falls below the noise level.

In the shallow-water case, bottom reflectance can be extracted from the ALB "real waveform" (optical signal), provided that the bottom return can be decoupled from the volume scattering. Two common methods for bottom return extraction are described below and their schematic plots are shown in Figure 5.4.3:

1) Extrapolation approach: The exponentially-decaying signal of the volume scattering return is extrapolated toward the trailing end of the waveform, extending over the time bins of the bottom return. The residual signal, which is the difference between the bottom return (in the original waveform) and the extrapolated curve is then used to estimate bottom return signal (Wang & Philpot, 2007).

2) Gaussian deconvolution: The bottom return signal is decomposed into several parametric curves. Symmetrical Gaussian functions are often employed for representing the surface (air/water interface) and bottom returns; exponentially modified Gaussian function have also been employed in situations where the asymmetry of the returns are not negligible (Cottin, Forbes, & Long, 2009; Wong & Antoniou, 1991, 1994)

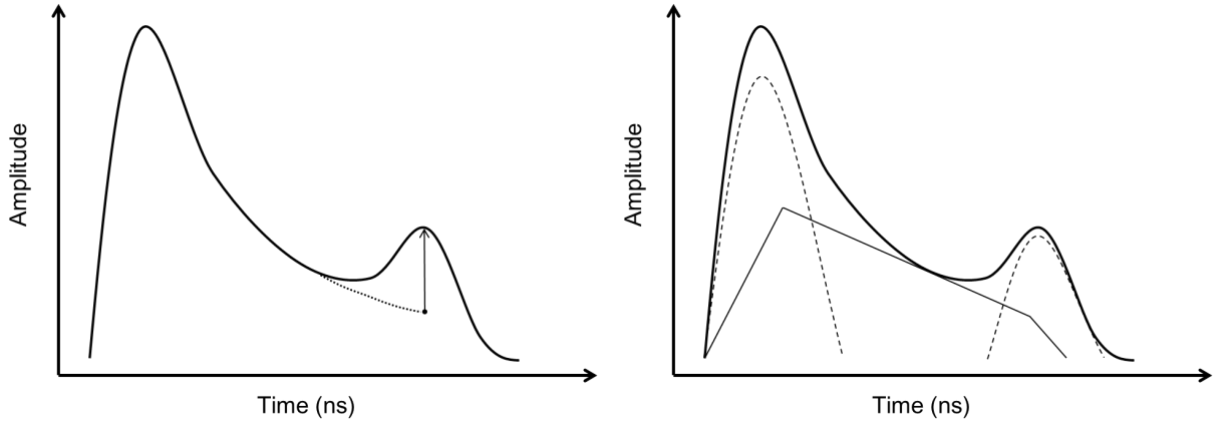

Figure 5.4.3. The schematic plots of extrapolation approach (left) and Gaussian deconvolution (right), where the water volume is modeled as a quadrilateral function, for bottom return extraction.

Modeling the water volume return is not trivial. As will be shown below, the modeling procedure can be well-described for a homogeneous water column; however, the assumption that the water column is vertically homogeneous is not always correct. Thus, linear, exponential, triangular, quadrilateral or successive Gaussian functions are all possible candidates for the modeling task (Abady, Bailly, Baghdadi, Pastol, & Abdallah, 2014; Collin et al., 2007; Wong & Antoniou, 1991). The selection of an appropriate function to model the volume scattering depends on the specific task of interest. The bottom return obtained by the Gaussian deconvolution approach provides a complete set of information, e. g., amplitude and shape, which can be useful for bottom classification. Nonetheless, the numerical instability and the computation cost are the major obstacles for conducting a Gaussian decomposition on ALB waveforms that contain a large number of laser measurements.

The bottom return power decreases in concert with the backscattered signal (see Figure 5.4.4). In order to obtain the bottom reflectance, the bottom return signals must be normalized to remove the water attenuation, which is described by the exponential factor [Section 5.3, Equation (4.3.1]:

$$\exp\left[2h_s^{bot} \cdot K_{sys}\left(h_s^{bot}\right)\right] \quad , \tag{4.4.1}$$

where h_s^{bot} is the slant bottom depth, and K_{sys} is the system attenuation coefficient described in details in Section 5.3. According to equation (5.3.4), the system attenuation coefficient may be expressed as:

$$K_{sys}\left(h_s^{bot}\right) = a_s - K'_{sys}\left(h_s^{bot}\right) = a_s - \ln F_D\left(h_s^{bot}\right) \quad , \tag{4.4.2}$$

where a_s is the effective absorption coefficient of the water, and the function F_D accounts for the effect of forward scattering of laser beam in the water on lidar signal decay with depth (Dolin and Levin 1991). The function is described in Sections 4.3.3 and 5.3). In the case of clear water and moderate depth, it is

important to note that the contribution from forward scattering to the system attenuation coefficient may be neglected for a lidar receiver with wide enough field-of-view. As a result, K_{sys} in equation (4.4.2) may be approximated (for homogeneous water column) by the effective absorption coefficient, a_s. Figure 5.4.4 provides an example for such a case (i.e., a nearly exponential signal decay $\sim\exp[-2h_s^{bot} \cdot a_s]$). In the extremely clear water ($a_s \approx 0.05\ m^{-1}$), the forward scattering effect does not manifest itself in the decay rate of the waveforms from the CZMIL "deep channel" up to the depth of ~ 40 m.

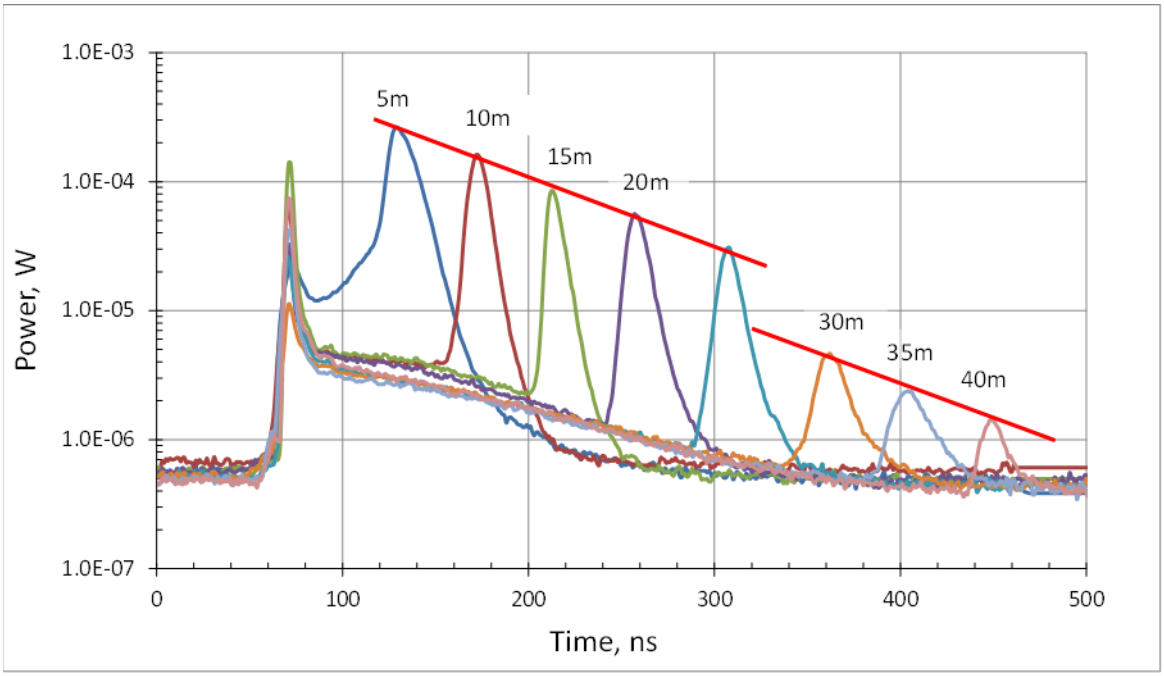

Figure 5.4.4. Attenuation of backscattered signal and bottom-reflected peaks at various depths. Superposition of waveforms from Fort Lauderdale coastal zone, Florida, obtained with CZMIL "deep channel" (PMT in "logarithmic" mode). The abrupt change in the magnitude of the bottom return between 25-30 m is indicative of a change in the water properties.

In the case under consideration (that is, in the situation when the forward scattering effect may be neglected), the exponential attenuation factor, $\exp[-2h_s^{bot} \cdot a_s]$, may be derived using an estimate of an effective absorption coefficient – assumed to be approximately constant throughout the water column – obtained from the lidar waveform as described in Section 4.3 above. The water attenuation factor can also be obtained by regression of the bottom return signals from a range of depths of the same bottom type. The latter method requires depth information and assumes that bottom composition and morphology are uniform over the survey area (Philpot, 1989). In the example shown in Figure 5.4.4 calculating the attenuation coefficient assuming a constant bottom reflectivity is valid for depths up to 25 m, but at greater depths the bottom reflectivity falls noticeably.

Earlier estimates of the bottom reflectance from SHOALS data were produced using a constant value of K_{sys} for the entire data set; specifically, an *a priori* value selected by the operator at the time of data acquisition was applied to the entire data set. Such estimates were called "pseudo-reflectance" (Lee & Tuell, 2003). In the more recent rapid environmental assessment (REA) processor of Optech, algorithms which estimate SHOALS K_{sys} for each waveform were implemented, and these values were used to

improve the pseudoreflectance of the dataset (Tuell et al., 2005). The improvement in the resulting bottom images proved to be significant for seafloor areas with varying morphology, such as a series of reefs separated by regions of sand, seagrass, and mixed vegetation (Tuell & Park, 2004).

Table 5.2. Values of lidar parameters and environmental characteristics used in the waveform simulation

Parameter & symbol	Units	Value
The lidar carrier height above the sea surface, *H*	m	400
The nadir angle in the atmosphere, $\boldsymbol{\theta_a}$	deg	20
The sounding beam divergence (full plane angle), $\boldsymbol{\Theta_E}$	mr	5
The receiver field-of-view (full plane angle)	mr	40
The pulse energy, *Q*	mJ	3
The effective sounding pulse duration (for 0.5 level), $\boldsymbol{\tau_R}$	ns	3.5
The bottom depth, $\boldsymbol{h^{bot}}$	m	20; 40
The effective absorption coefficient, $\boldsymbol{a_s}$	m-1	0.075
The forward scattering coefficient, $\boldsymbol{b_s}$	m-1	0; 0.2
The VSF shape parameter in Dolin's model, $\boldsymbol{m}$	-	7
The water surface reflectance, $\boldsymbol{\rho_{sf}}$	-	0.002
The bottom reflectance, $\boldsymbol{\rho_{bot}}$	-	0.15

In the general case (e.g., for more turbid waters), forward scattering of the sounding light beam may seriously affect the applicability of the above approach for bottom reflectance estimation. The impacts of forward scattering include: (1) departure of the waveform decay rate from a purely exponential dependence, $\sim exp[-2h_s \cdot a_s]$, and (2) a stretch of the bottom-reflected pulse caused by the spread of the sounding laser beam (Tuell et al., 2005). The effects are illustrated in Figure 5.4.5 through Figure 5.4.8 using simulated waveforms obtained with the CZMIL simulator (Section 4.3.3) and the lidar waveform model described in Section 4.3.2. The values of the lidar parameters and environmental characteristics used in the simulation are listed in Table 5.2.

The effect of forward scattering in the water on the waveform decay rate was discussed in Section 5.3 (Figure 5.3.2). Neglecting the waveform decay rate effect (in the case of deep / turbid enough water) will lead to underestimate of the bottom return decrease with depth, and a corresponding error in normalization of the bottom return signal for attenuation by the water column [Section 5.3, Eq. (4.3.1)]. As a result, bottom reflectance may be overestimated. In Figure 5.4.5 (forward scattering coefficient, b_s= 0.2 m^{-1}), the error does not exceed ~20%, at 20 m depth. However, for the deeper water example in Figure 5.4.6; (depth 40 m, $b_s = 0.2\ m^{-1}$), the error reaches up to 200%.

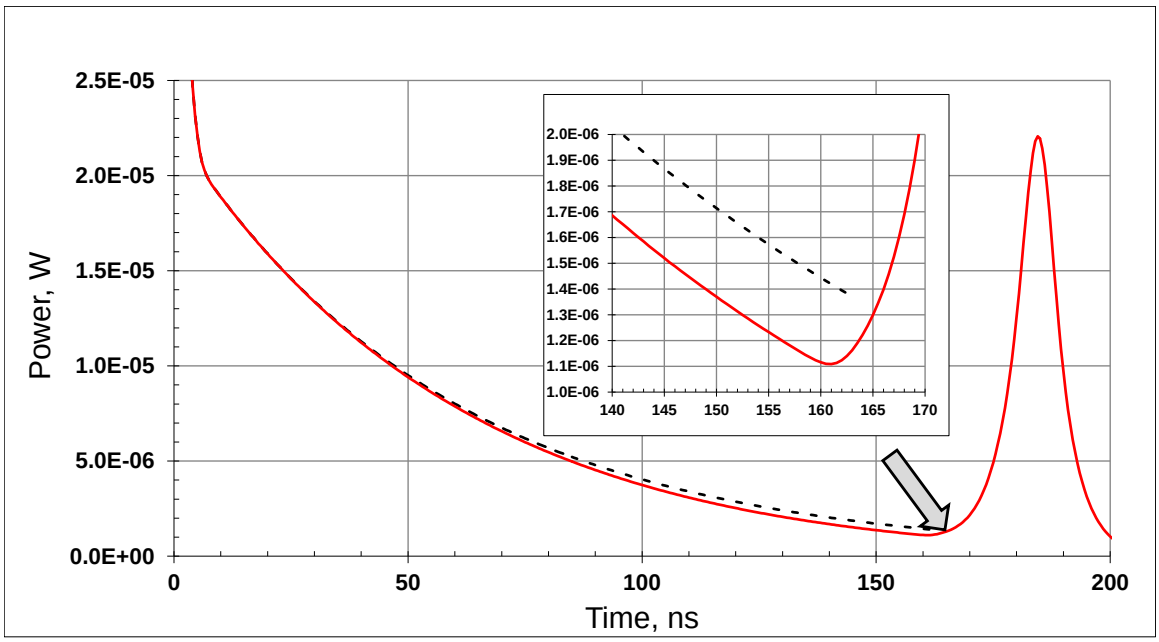

Figure 5.4.5. Simulated CZMIL deep channel waveform for a bottom depth of 20 m. The red, solid line is the waveform calculated for the forward scattering coefficient, $b_{sf} = 0.2\ m^{-1}$; the black line corresponds to zero forward scattering ($b_s = 0\ m^{-1}$) and demonstrate the "pure exponential" decay of backscattered signal, $\sim exp[-2h_s \cdot a_s]$.

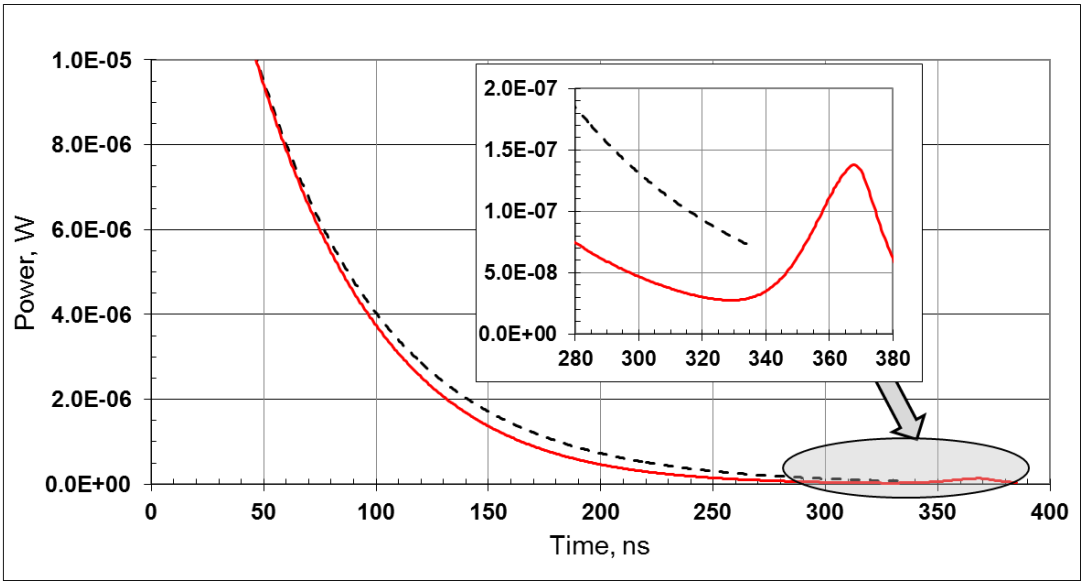

Figure 5.4.6. Simulated CZMIL deep channel waveform for a bottom depth of 40 m. Red, solid line is the waveform calculated for the forward scattering coefficient $b_s = 0.2\ m^{-1}$; black, dashed line corresponds to zero forward scattering, $b_s = 0\ m^{-1}$, and demonstrate "pure exponential" decay of the backscattered signal, $\sim exp[-2h_s \cdot a_s]$.

Figure 5.4.8 and Figure 5.4.9 demonstrate the bottom-reflected pulse stretch due to small-angle forward scattering of the laser beam in water (the "environmental stretch"). The stretch reduces the amplitude of bottom return. If the pulse stretch is not taken into account, the result may lead to significant underestimation of bottom reflectance. The pulse stretch effect increases with depth and water turbidity

eCommons (2019) https://doi.org/10.7298/98sb-4t84

(with the forward scattering coefficient, b_f). The "environmental stretch" is observed against the background stretch of the reflected peak due to the ray-path geometry ("geometrical stretch", Section 4.2.1) and the effective pulse duration ("hardware-based stretch", Section 4.2.2). Therefore, the effect of "environmental stretch" is the less prominent with wider effective pulses or at greater off-nadir (incidence) angles.

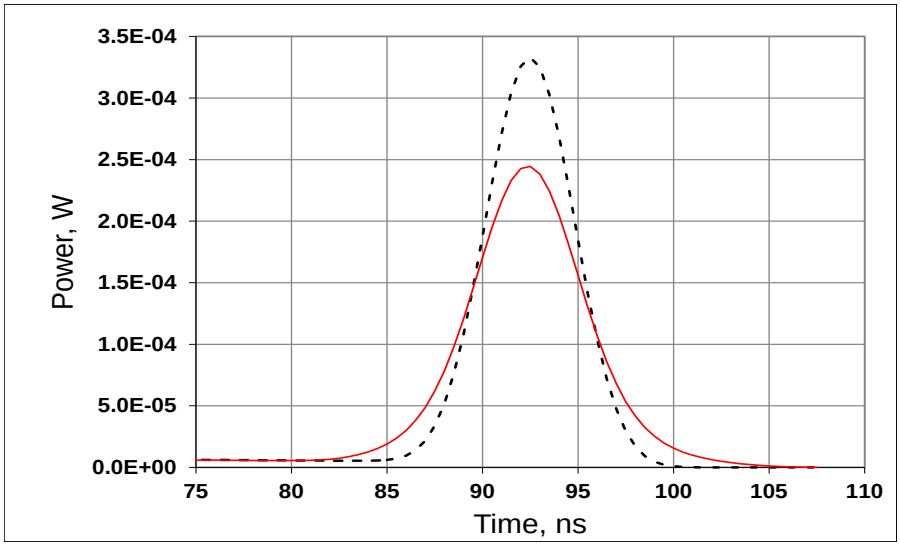

Figure 5.4.7. A simulated CZMIL deep channel waveform over the time interval of the bottom-reflected signal for a bottom depth of 10 m. The black, dashed line corresponds to zero forward scattering (b_s= 0 m-1), when the shape of bottom peak is determined only by the "geometric" and the "hardware-based" stretch. The red, solid line depicts the waveform calculated for the forward scattering coefficient b_s= 0.2 m-1 and demonstrates the additional "environmental stretch" of the peak.

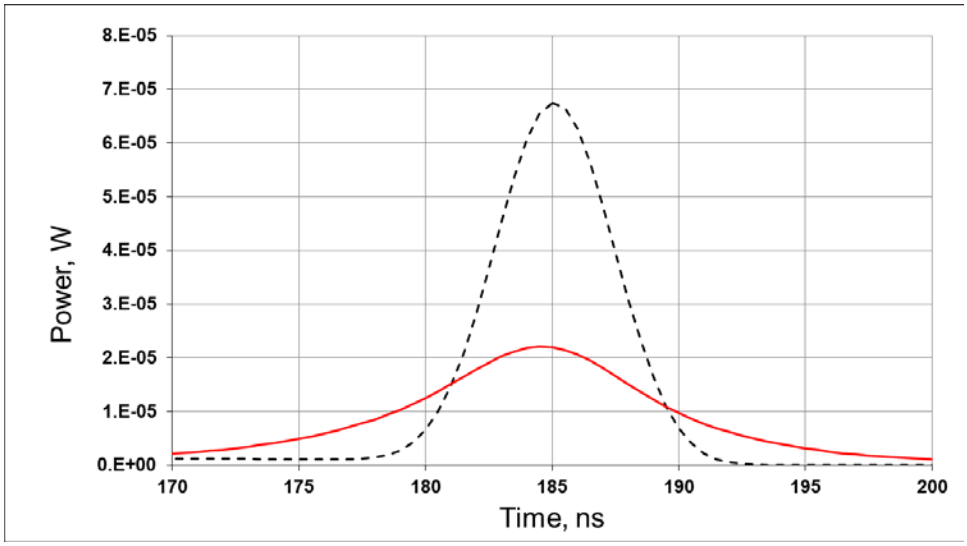

Figure 5.4.8. Simulated CZMIL deep channel waveform in the time interval of bottom-reflected signal for the bottom depth of 20 m. The black, dashed line corresponds to zero forward scattering ($b_s = 0\ m^{-1}$), when the shape of bottom peak is determined only by "geometric" and "hardware-based" stretch. The red, solid line depicts the waveform calculated for the forward scattering coefficient, $b_s = 0.2\ m^{-1}$, and illustrates the additional "environmental stretch" of the peak.

To summarize, bottom return signals need to be inverted using an estimate of the water attenuation (Equation (4.4.1) in order to obtain bottom reflectance. The water attenuation coefficient can be obtained either by the regression of the bottom return signals over range of depths of the same bottom type or from the water volume return as a result from the waveform decomposition method. Previous studies for extracting bottom reflectance required depth information and assumes that bottom composition and morphology are uniform over the survey area.

Caution must be exercised when compiling bottom reflectance maps using several flight lines. Environmental factors, such as water surface and bottom slopes may affect the reflectance estimation (Section 3.4). The light field is continuously varying over the transmission and return path (Section 5.3). Also, the laser beam undergoes focusing as the laser pulse enters the water, and defocusing as the return pulse exits the water. As a consequence, the magnitude and variability of the bottom return signal initially increases as the water depth decreases and may reach maximum values at a depth that is related to the water surface geometry. This is the phenomenon of double focusing (Abrosimov & Luchinin, 1999; Luchinin, 1987; McLean & Freeman, 1996)). Wang and Philpot (2007) showed using data from a study site near Egmont Key, FL, that the effect of double focusing can be reduced in turbid water. Nonetheless, the asymmetric shape of the water surface, typically in coastal areas, alters the light field differently for adjacent survey flight lines. As a result, the estimated bottom reflectance over the same area may have different values for adjacent survey flight lines.

It is also important to note that bottom slope affects the shape of the bottom return, where the pulse is more stretched with increasing angle of incidence (Steinvall & Koppari, 1996). The benefit of employing the waveform decomposition method is that the complete information of the bottom return in that the shape of the bottom return is appropriately depicted by the Gaussian. On the other hand, using the peak value of the bottom return signal requires that the signal correction must rely on other simulation results or experiments (Tulldahl & Wikström, 2012; Wang & Philpot, 2007).

5.5 Effects of forward scattering

Minsu Kim

When a laser pulse propagates through an attenuating (absorbing and scattering) medium, environmental parameters control the varying rate of the decreasing return, and may deform the position and shape of the surface reflection and bottom reflection peaks of the ALB waveform. Since these are used for estimating depth, the deformations introduce uncertainties in the depth estimate. The environmental parameters include atmosphere, air-water interface, water body, and the bottom surface characteristics. As will be demonstrated in this section, the most prominent factor among the environmental parameters is the scattering coefficient. Other environmental factors add only minor variations to that of the main scattering effect. Accordingly, we describe the scattering effect first and, since the scattering coefficient cannot vary independently from other inherent optical properties (IOPs), we introduce a single formula that constrains several inherent optical properties.

5.5.1 Effect of scattering and inherent optical properties

As described in Section 3.3.2, it is possible to derive several environmental parameters using two fundamental IOPs, the absorption coefficient, a, and the volume scattering function (VSF). The scattering

coefficient, b, is obtained by integrating the VSF over the all possible directions (equation (3.3.7)). The lidar backscattering coefficient, β_π (a.k.a. beta pi), is the value of the VSF in the exact backward direction. The degree of forward scattering – which is critical for understanding the beam spread – is also determined from the VSF. While it is possible that one parameter can vary independently of the other parameters, it is generally most reasonable to simulate IOPs assuming that they are mutually constrained. There is no unique relationship among IOPs, however, for convenience, we simulate IOPs with the following simple formula: we assume that the single scattering albedo (equation (3.3.16)), $\omega_0 = b/(a+b)$, is constant and that the lidar backscattering coefficient is determined by the scattering coefficient via $\beta_\pi = 0.005 \cdot b$.

Figure 5.5.1 illustrates waveforms computed using sets of IOPs for which the constant single-scattering albedo is 0.7, the scattering coefficient varies from 0.2 to 0.5 m^{-1}, and the rest of IOPs are derived using the formulas above. Based on simulation results, we are able to observe several fundamental characteristics of the waveforms:

- As the scattering coefficient increases the bottom return is reduced dramatically due to the exponential increase in attenuation.
- In relatively clear water ($K_d(532nm) < 0.1m^{-1}$), the loss of laser pulse energy during propagation is due primarily to absorption.
- Scattering becomes increasingly dominant as the water becomes more turbid, and can become comparable to absorption in its contribution to attenuation.
- Backscattering has a relatively minor effect on the returns compared to absorption and forward scattering; the increased attenuation of the ALB returns is due primarily to forward scattering, spreading the beam as it propagates through the scattering medium, and redistributing the beam energy over the beam cross-sectional area.
- The increase in attenuation with increasing scattering is particularly noticeable in the last 2/3 of the waveform. The bottom reflectance return decreases correspondingly.

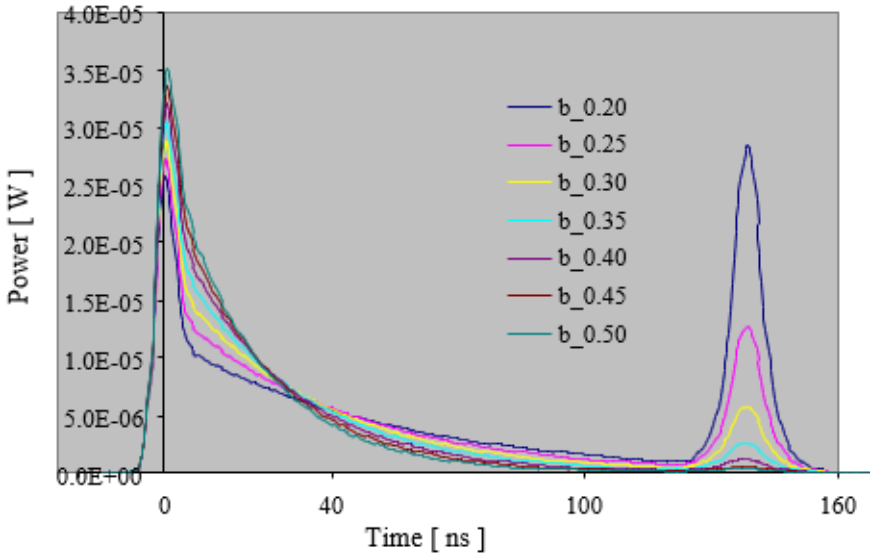

Figure 5.5.1. Changes in waveforms from 15 m deep water due to changes in the scattering coefficient (ranging from 0.2 to 0.5 m^{-1}) and related IOPs.

In order to investigate the effect of variation in the IOPs on the lidar depth accuracy, we also simulated the optical properties affecting the surface and bottom return. The Fresnel peak (fixed value) and the different backscatter curves are shown in Figure 5.5.2a. The combined Fresnel + backscatter curves are shown in Figure 5.5.2b. In both figures, the true geometrical position of the water surface is marked as a solid line at time 0 ns.

It is important to note that the magnitude and position of the peak of the surface return is determined by two factors: the effective Fresnel reflectance and the lidar backscattering coefficient. In the simulation results shown in Figure 5.5.1, the effective Fresnel reflectance is constant, and the backscattering coefficient increases linearly with the scattering coefficient values. The superposition of a fixed, pure Fresnel peak and increasing volume backscattering has two consequences: greater peak magnitude and the shift of the maximum position to a later time (Figure 5.5.2b)

Note also, that the surface return signal increases as the scattering coefficient increases because of the increased backscattering near the surface. However, as the laser pulse propagates through the medium, however, it loses intensity much more quickly because so much energy has been lost due to the high scattering and absorption. This is the reason for the apparent convergence of the curves near 30 ns in (Figure 5.5.2a).

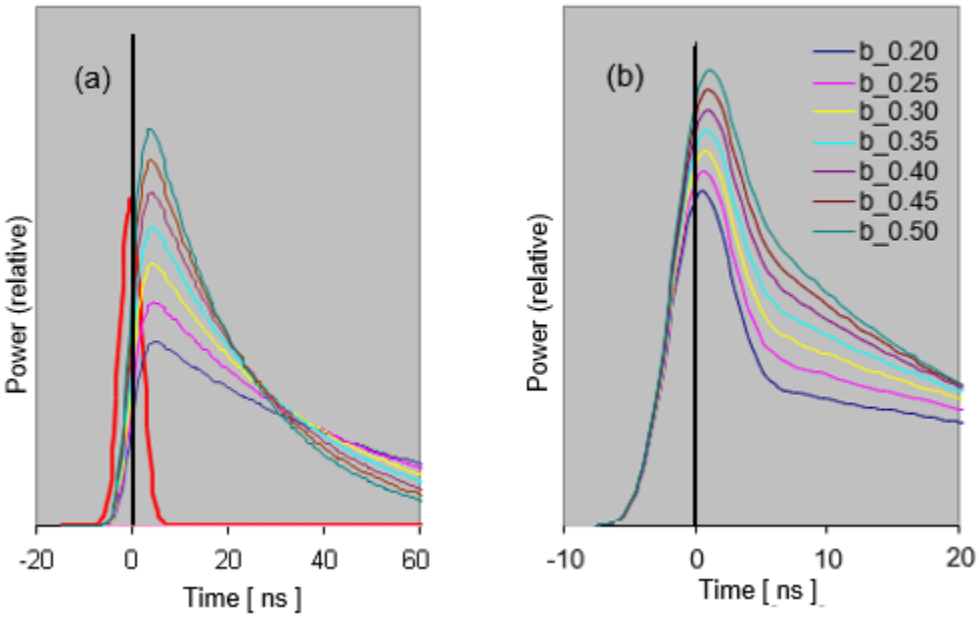

Figure 5.5.2. Details of surface return data from Figure 5.5.1: (a) Fresnel peak (thick red line) and the variable volume backscattering; (b) superposition of the two components.

The bottom return peak also experiences a shift due to scattering dispersion. In Figure 5.5.3 the bottom peaks were normalized by the bottom peak energy (integrated power over the duration of bottom peak) in order to facilitate comparison. Clearly, the increase in the scattering coefficient, and the corresponding IOPs, not only lowers the magnitude of the bottom peak, but also shifts the peak position to an earlier time. The shift can be explained as follows. A laser pulse approaching the bottom at a substantial optical depth will have broadened significantly due to forward scattering. The increase in the rate of dispersion with optical depth is significant, so that, when a beam front intersects the bottom boundary, the later part

of the beam front (farther from the laser source) experiences more dispersion than the earlier part of the beam front (see Figure 4.2.4). The later signal is also further attenuated by absorption. As a result, the bottom peak always occurs earlier than the true geometric bottom (at 140 ns), defined as point at which the beam center meets the bottom.

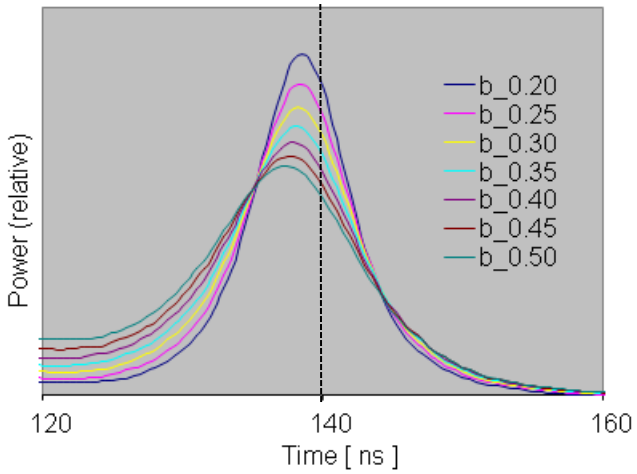

Figure 5.5.3. Normalized bottom peaks using the bottom peak energy Lidar depth estimation algorithm

5.5.2 Lidar depth estimation algorithm

When a lidar waveform is generated by a laser pulse at a slant incidence angle, the slant distance between the two peaks is used as a close approximation to the true slant distance. An intuitive method to calculate the slant distance is based on the time separation of the two apparent peaks which we will call the "peak algorithm". Another common practice is to calculate the distance based on the time separation of the two half-peaks where the waveform value is the half of the maximum, or the "half-peak algorithm". With the peak algorithm it is assumed that the peaks occur close in time to the real surface and the bottom peaks. If the overall system response is short enough – having a short laser pulse duration, fast photo-detector and electronic response, and small incident angle for minimal geometrical stretch – the peak algorithm is an ideal approach. As these conditions are violated more and more, the peak algorithm will be subject to be subject to greater depth estimation errors.

The key assumption in the half-peak algorithm is that the two peaks have the same width; however, different factors contribute to the widths of the two peaks. The geometric stretch of the surface peak is a combination of many system factors, such as beam divergence angle, receiver FOV, sensor altitude, and system response function. At shallow depths, the effective beam divergence angle and the FOV both decrease according to Snell's law, after refraction at the water surface. The width of the resulting bottom and surface return may be quite similar, despite the dispersion due to scattering. However, the ALB beam spreads rapidly as the optical depth increases, leading to significant stretching of the bottom return. Thus, depth estimation error for the half-peak algorithm will be closely related to the beam dispersion due to forward scattering.

As an example of the two approaches, consider a model in which the two peaks of a waveform are represented using a Gaussian curve, with the FWHM being the measure of the peak width. In this

example, both the peak algorithm and the half-peak algorithm exhibit an increasing bias from the true surface arrival time, as illustrated in Figure 5.5.4.

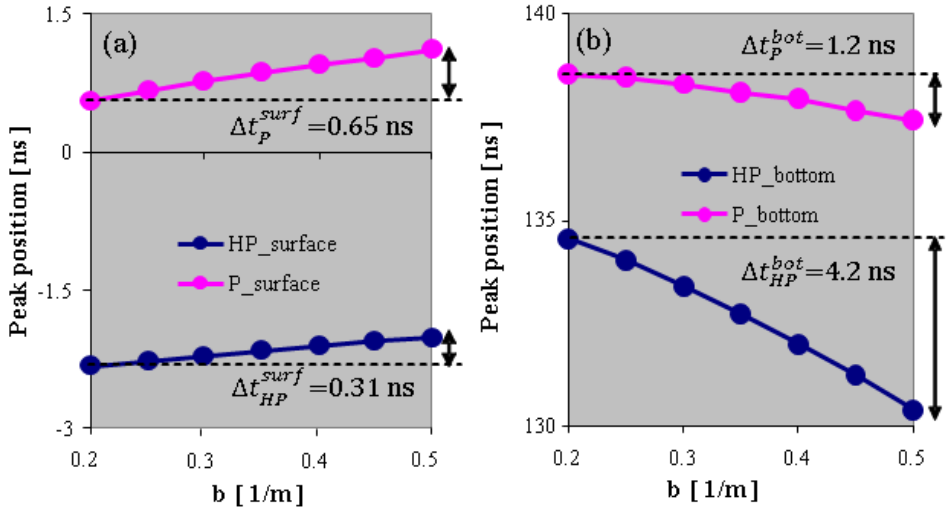

Figure 5.5.4. Bias of estimates relative to the true locations of (a) the surface (Δt_P^{surf} and Δt_{HP}^{surf}), and (b) the bottom (Δt_P^{bot} and Δt_{HP}^{bot}), using the peak algorithm (P) and the half-peak algorithm (HP) as the scattering coefficient increases. The dashed lines represent the arrival times at the surface and bottom along the slant path.

As the scattering coefficient increases (along with corresponding changes in the other IOPs), both the peak and half-peak estimates of the surface arrival time shift toward a later time. For $b = 0.5\ m^{-1}$, the position shift for the peak algorithm is slightly more than that of the half-peak algorithm. In contrast, the estimate of the bottom peak location shifts to an earlier time for both algorithms. For the same conditions, the bottom peak shift is about twice the surface peak shift; however, the half-peak shift of the bottom location is more than 10 times the surface half-peak shift. The combined error when $b = 0.5\ m^{-1}$ is a 1.8 ns bias for the peak algorithm, while for the half-peak algorithm the combined error is a 4.5 ns bias. The increased total error demonstrates the greater vulnerability of the half-peak algorithm to beam dispersion by forward scattering. Depth estimation errors using the 2 algorithms for varying IOPs are calculated for several depths in Figure 4.5.5.

The time difference (Δt) between two peak positions or half-peak positions is converted to the depth error, Δd, using the simple formula

$$\Delta d = \left(\frac{c}{2n_w}\right) \Delta t \cos\theta_w \quad , \tag{4.5.1}$$

where θ_w is the incidence (sounding) angle in water. The resulting depth estimation error using the peak algorithm is much smaller than the error produced using the half-peak algorithm.

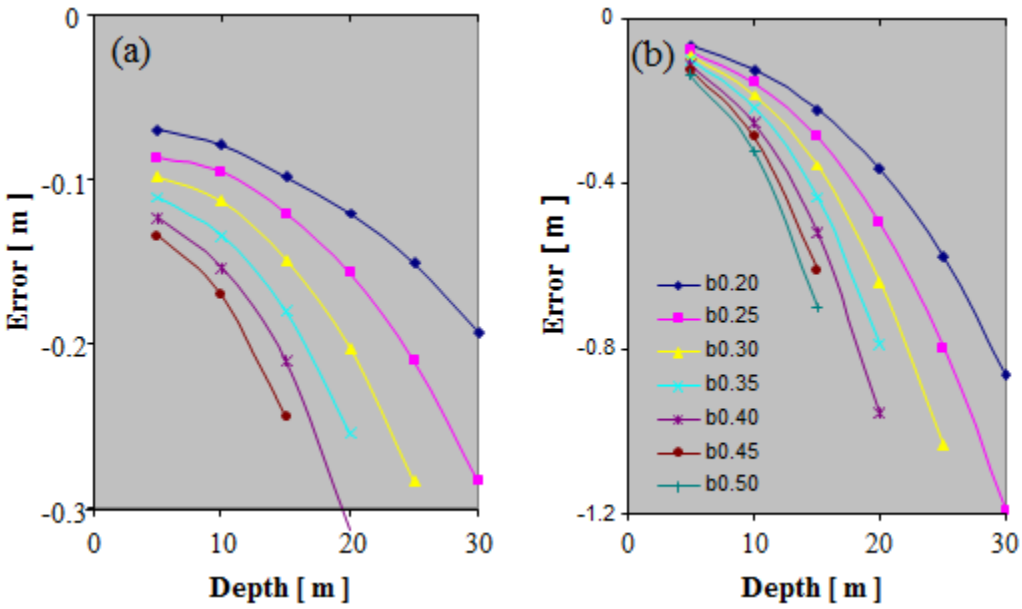

Figure 5.5.5. Depth error for varying IOPs using (a) Peak and (b) Half-Peak algorithm.

5.5.3 Effect of the effective surface Fresnel reflectance

Under most conditions (other than flat calm) there are many small facets of the complicated surface wave structure aligned such that a small portion of the laser pulse will be specularly reflected back to the receiver (Section 3.2). The effective Fresnel reflectance is then related to the probability of specular reflection. If the entire water surface were perpendicular to the beam axis, the effective Fresnel reflectance would be near 0.02 which is the Fresnel reflectance due to the normal incidence to the water with refractive index $n_w = 1.33$. Thus, 0.02 is the theoretical maximum. Of course, if the water surface is covered with white caps due to breaking waves, the effective Fresnel reflectance can be much higher, but such a case is not considered.

Figure 5.5.6a illustrates a set of waveforms produced using a range of effective Fresnel reflectance values; Figure 5.5.6b is a close-up of the surface peak region. The surface peak is the sum of the effective Fresnel reflectance and the volume backscattering. When the effective Fresnel reflectance is low, the contribution to the apparent surface peak by the surface reflection is small and the apparent surface peak occurs significantly later than the time when the true center of the beam passes the water surface. With high effective Fresnel reflectance, however, the surface peak is dominated by the Fresnel reflectance, and the apparent peak position occurs very close to the time when the true center of the beam passes the surface.

eCommons (2019) https://doi.org/10.7298/98sb-4t84

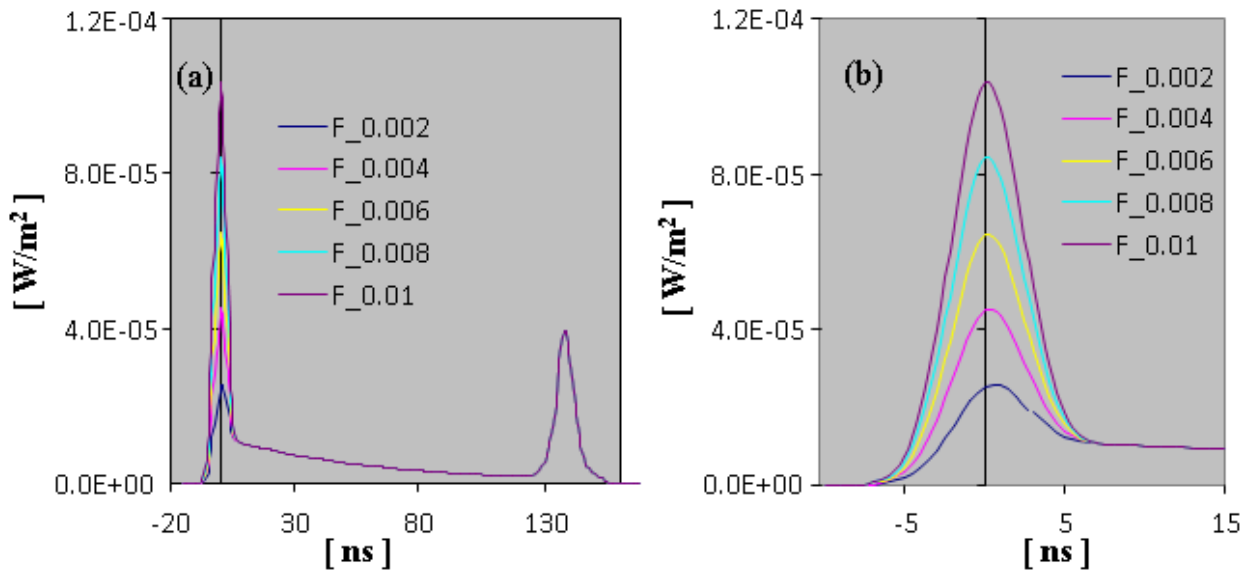

Figure 5.5.6. Waveforms for varying effective Fresnel reflectance.

An increase in the effective Fresnel reflectance has the effect of increasing the error in the depth calculation (Figure 5.5.7). As with the effect of IOPs on the surface peak, the error introduced by the peak algorithm is less than half of that introduced by the half-peak algorithm. On the other hand, the variation in the depth estimate produced by the half-peak position is less than that of the peak position. Thus, the depth error plot using the peak algorithm (Figure 5.5.7a) shows a wider range of error for varying effective Fresnel reflectance than the half-peak algorithm (Figure 5.5.7b) at any one depth. Interestingly, the range of uncertainties is nearly constant for any one depth when using the half-peak algorithm. This is because the effective Fresnel reflectance affects only the near surface part of the waveform. Thus, the bottom peak is not affected by the Fresnel reflectance regardless of the depth.

The greatest apparent trend with increasing depths is due to the effect of beam dispersion due to scattering. As a result, the bottom peak stretching affects the depth error. To demonstrate this idea, we can generate a new error plot using a larger scattering coefficient. The first group of data was simulated using $b = 0.2\ m^{-1}$.. The new data set was simulated using $b = 0.4\ m^{-1}$. Figure 5.5.8 shows two groups of error plots. It is evident that the Fresnel variation explains the width of the band and that the overall trend is due to the scattering. The upper group is for $b = 0.1\ m^{-1}$ and the lower group is for $b = 0.2\ m^{-1}$.

eCommons (2019) https://doi.org/10.7298/98sb-4t84

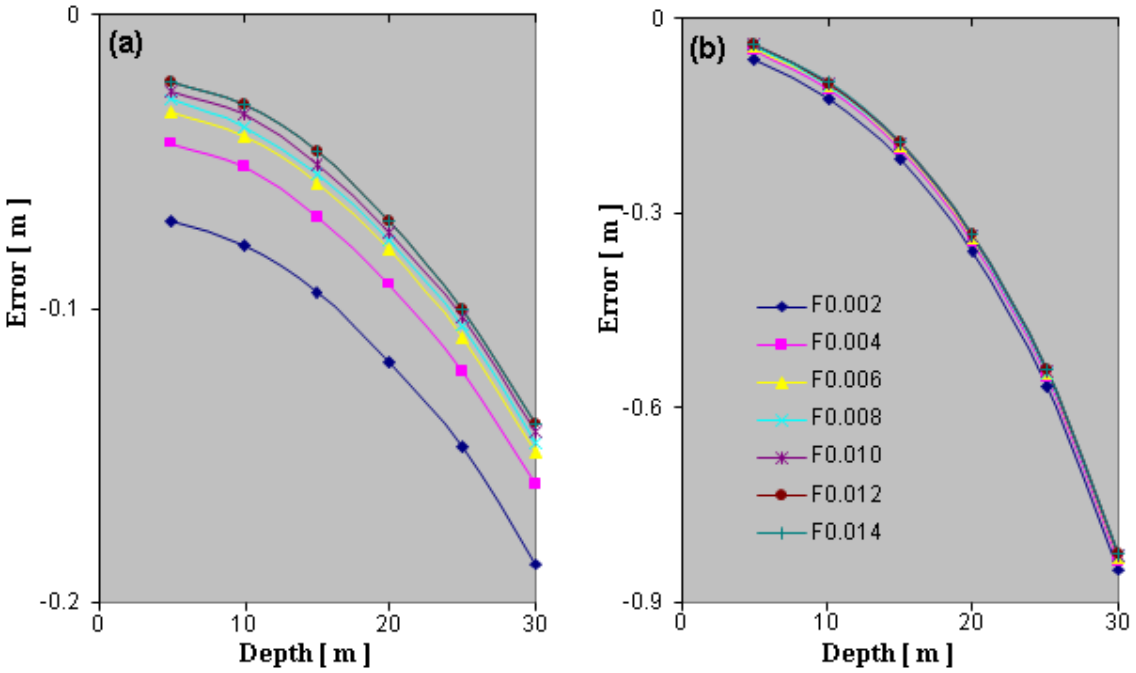

Figure 5.5.7. Depth estimation error for varying effective Fresnel reflectance using (a) Peak and (b) Half-Peak algorithm. Note that the overall error of the peak algorithm is much less than the half-peak algorithm, and that the spacing of the peak curves (a) is nearly independent of depth while the half-peak curves (b) converge with increasing depth.

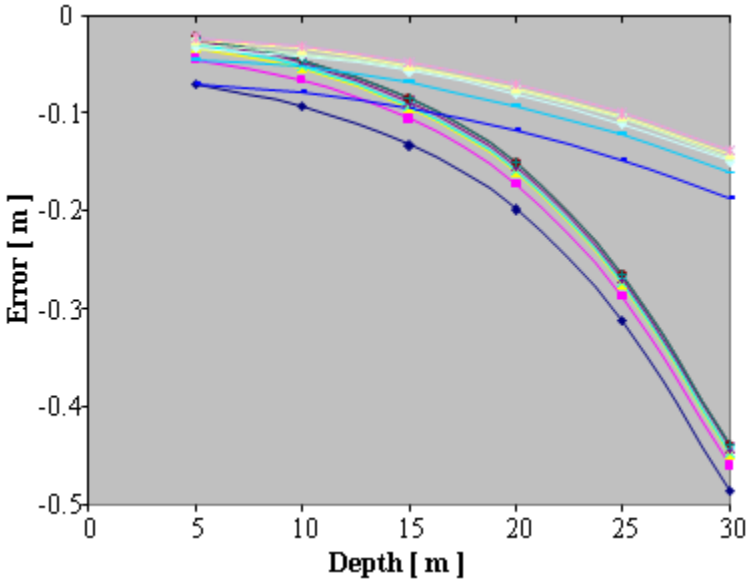

Figure 5.5.8. Effect of the Fresnel reflectance for 2 different scattering coefficient. The upper group of curves is for b = 0.1; the lower group is for b = 0.2.

5.5.4 Effect of the bottom reflectance

A change in bottom reflectance affects nothing but the bottom peak; the surface return and the volume backscattering return are invariant while the bottom peak rises as the bottom reflectance increases. The effect is illustrated in Figure 5.5.9 in which the bottom peak represents the sum of the pure bottom peak and the volume backscattering. Since the volume backscattering is constant, the increase in bottom reflectance results in a bottom peak that is more representative of the bottom, resulting in a shift of the apparent peak or half-peak closer to the true values. The peak and half-peak positions are marked as dots in Figure 5.5.9b. Both peak and half-peak positions are delayed as the bottom reflectance increases and as the pure bottom peak becomes stronger than volume backscattering base. Convergence occurs rather quickly. It is worth keeping in mind, however, that even the strongest bottom peak position is still affected by the scattering attenuation, so that the converged peak is optically shifted from the true geometrical bottom (see Figure 5.5.3). As mentioned in the IOPs section, an overall quick increase of depth estimation error over the increasing depth is caused by the beam stretch of the forward scattering. Thus, the error caused by the bottom reflectance variation is represented by the small differences between the curves in Figure 5.5.10.

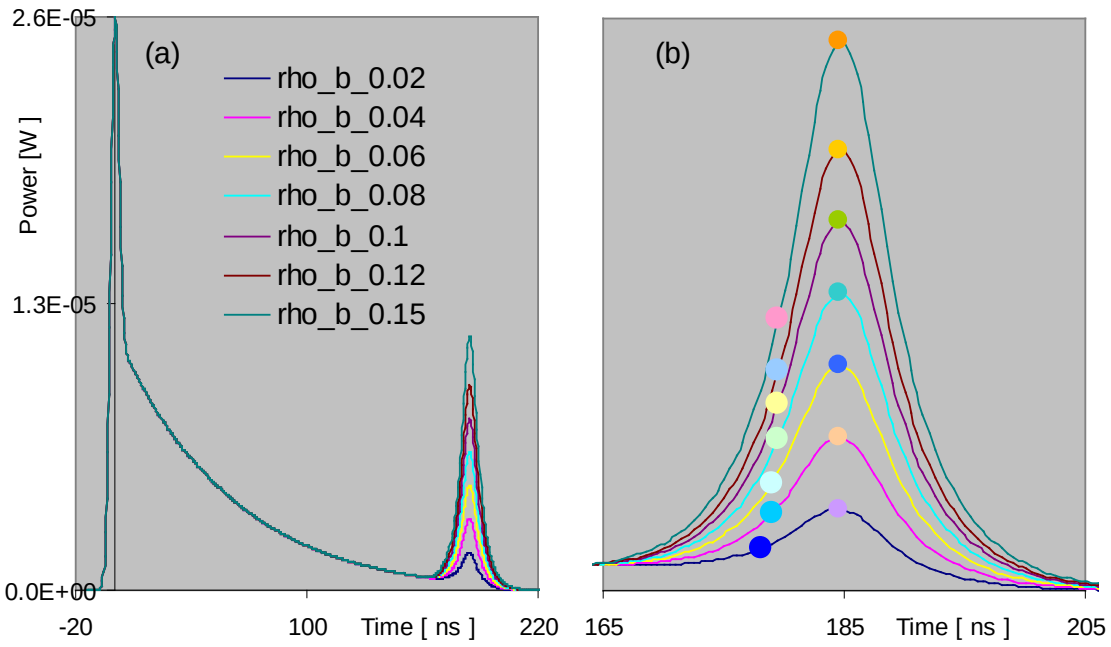

Figure 5.5.9. The effect of increasing bottom reflectance: a) full waveform, b) detail of the bottom peak with the peak and half-peak positions marked as dots.

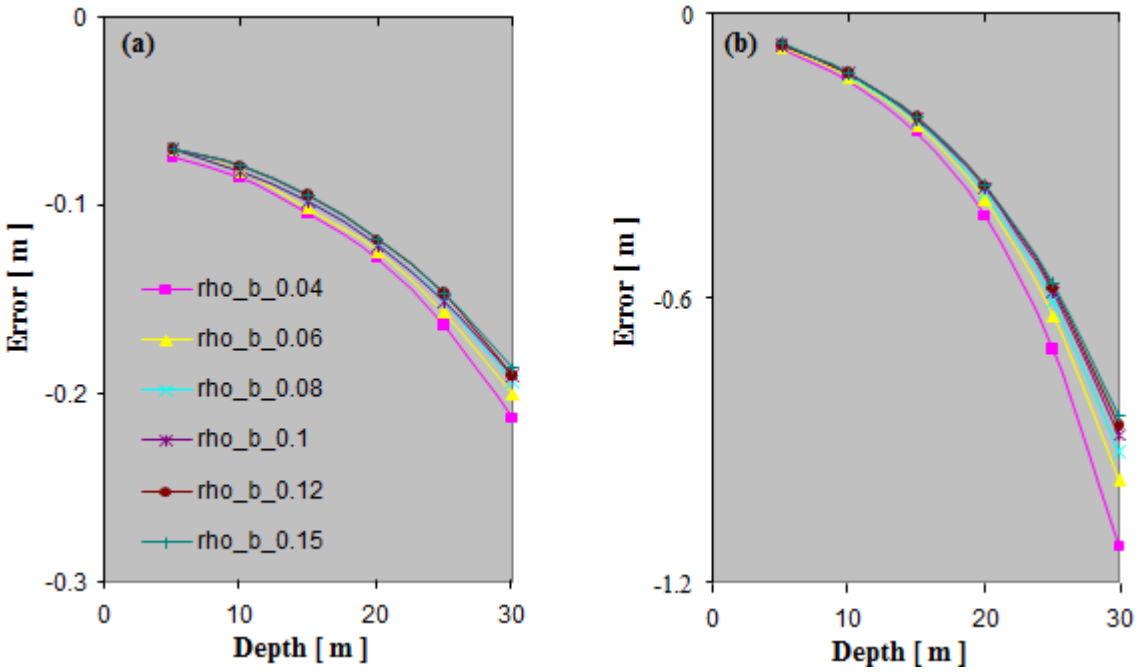

Figure 5.5.10. Depth error for varying bottom reflectance using (a) Peak and (b) Half-Peak algorithm.

5.6 References

Abady, L., Bailly, J.-S., Baghdadi, N., Pastol, Y., & Abdallah, H. (2014). Assessment of Quadrilateral Fitting of the Water Column Contribution in Lidar Waveforms on Bathymetry Estimates. *Geoscience and Remote Sensing Letters, IEEE*, *11*(4), 813–817. https://doi.org/10.1109/LGRS.2013.2279271

Abrosimov, D. L., & Luchinin, A. G. (1999). Signal statistics of lidar sounding of the upper ocean through its rough surface. *Izvestiya, Atmospheric and Oceanic Physics (in Russian)*, *35*, 266–272.

Collin, A., Cottin, A. G., Long, B. F., Kuus, P., Clarke, J. H., Archambault, P., … Miller, J. (2007). Statistical classification methodology of SHOALS 3000 backscatter to mapping coastal benthic habitats. In *2007 IEEE International Geoscience and Remote Sensing Symposium, IGARSS 2007, June 23, 2007 - June 28* (pp. 3178–3181). Department of Geology, INRS-ETE, University of Quebec, QC, Canada: Institute of Electrical and Electronics Engineers Inc. https://doi.org/10.1109/IGARSS.2007.4423520

Cottin, A. G., Forbes, D. L., & Long, B. F. (2009). Shallow seabed mapping and classification using waveform analysis and bathymetry from SHOALS lidar data. *Canadian Journal of Remote Sensing*, *35*(5), 422–434.

Dolin, L. S., & Levin, I. M. (1991). *Reference book on the underwater vision theory*. Leningrad: Gidrometeoizdat Press (in Russian).

Dolin, L. S., & Savel'ev, V. A. (1971). Characteristics of the backscattering signal and pulse radiation of turbid media by a narrow directional light beam. *Atmospheric and Oceanic Physics*, *7*(5), 505–510.

Dorogin, A. N., Kopelevich, O. V., Levin, I. M., & Feigels, V. I. (1988). Correlation among some hydrooptical properties. In *Optics of the sea and the atmosphere (in Russian)* (pp. 136–137). Academy of Science of the USSR.

Lee, M., & Tuell, G. H. (2003). A technique for generating bottom reflectance images from SHOALS data. In *U.S. HYDRO 2003*. New Orleans, LA.

Levin, I. M., & Kopelevich, O. V. (2003). Relationships between seawater optical properties at 550 nm. In I. M. Levin & G. D. Gilbert (Eds.), *Current Probles in Optics of Natural Waters (ONW 2003)*. St. Petersburg, Russia.

Luchinin, A. G. (1987). Some properties of a backscattered signal in laser sounding of the upper ocean through a rough surface. *Izvestiya, Atmospheric and Ocean Physics (in Russian)*, *23*, 725–729.

McLean, J. W., & Freeman, J. D. (1996). Effects of ocean waves on airborne lidar imaging. *Applied Optics*, *35*(18), 3261–3269. https://doi.org/10.1364/AO.35.003261

Mobley, C. D. (1994). *Light and water: radiative transfer in natural waters*. San Diego: Academic Press. Retrieved from http://www.curtismobley.com/LightandWater.zip

Monin, A. S. (1983). Physical optics of the ocean. In A. S. Monin (Ed.), *Ocean Optics* (Vol. 1). Nauka, Moscow (in Russian).

Morel, A., & Loisel, H. (1998). Apparent Optical Properties of Oceanic Water: Dependence on the Molecular Scattering Contribution. *Applied Optics*, *37*(21), 4765–4776. https://doi.org/10.1364/AO.37.004765

Park, J. Y., Ramnath, V., Feygels, V. I., Kim, M., Mathur, A., Aitken, J., & Tuell, G. H. (2010). Active-passive data fusion algorithms for seafloor imaging and classification from CZMIL data, 769515. Retrieved from http://dx.doi.org/10.1117/12.851991

Pe'eri, S., & Philpot, W. D. (2007). Increasing the existence of very shallow-water LIDAR measurements using the red-channel waveforms. *IEEE Transactions on Geoscience and Remote Sensing*, *45*(5), 1217–1223. https://doi.org/10.1109/TGRS.2007.894584

Philpot, W. D. (1989). Bathymetric mapping with passive multispectral imagery. *Applied Optics*, *28*(8), 1569–1578. https://doi.org/10.1364/AO.28.001569

Smart, J. H., & Kwon, K. H. K. (1996). Comparisons between in-situ and remote sensing estimates of diffuse attenuation profiles. In V. I. Feigels & Y. I. Kopilevich (Eds.), *SPIE 2964: Laser Remote Sensing of Natural Waters: From Theory to Practice* (Vol. 2964, pp. 100–109). International Society for Optics and Photonics. https://doi.org/10.1117/12.258356

Steinvall, O. K., & Koppari, K. R. (1996). Depth sounding lidar: An overview of Swedish activities and future prospects. In V. I. Feigels & Y. I. Kopilevich (Eds.), *CIS Selected Papers: Laser Remote Sensing of Natural Waters: From Theory to Practice* (Vol. SPIE 2964, pp. 2–25). St. Petersburg, Russia: SPIE. https://doi.org/10.1117/12.258342

Steinvall, O. K., Koppari, K. R., & Karlsson, U. C. M. (1993). Experimental evaluation of an airborne depth-sounding lidar. *Optical Engineering*, *32*(6), 1307–1321. https://doi.org/10.1117/12.135859

Tuell, G. H., Feygels, V. I., Kopilevich, Y. I., Weidemann, A. D., Cunningham, A. G., Mani, R., … Aitken, J. (2005). Measurement of ocean water optical properties and seafloor reflectace with scanning hydrographic operational airborne lidar survey (SHOALS): II. Practical results and comparison with independent data. In R. J. Frouin, M. Babin, & S. Sathyendranath (Eds.), *SPIE 5885: Remote Sensing of the Coastal Oceanic Environment, July 31- August 1, 2005* (Vol. 5885, pp. 58850E-58850E – 13). San Diego, CA: SPIE. https://doi.org/10.1117/12.619215

Tuell, G. H., & Park, J. Y. (2004). Use of SHOALS bottom reflectance images to constrain the inversion of a hyperspectral radiative transfer model, 185–193. Retrieved from http://dx.doi.org/10.1117/12.564929

Tulldahl, H. M., & Wikström, S. A. (2012). Classification of aquatic macrovegetation and substrates with airborne lidar. *Remote Sensing of Environment*, *121*, 347–357. https://doi.org/10.1016/j.rse.2012.02.004

Wang, C.-K., & Philpot, W. D. (2007). Using airborne bathymetric lidar to detect bottom type variation in shallow waters. *Remote Sensing of Environment*, *106*(1), 123–135. https://doi.org/10.1016/j.rse.2006.08.003

Wong, H., & Antoniou, A. (1991). Characterization and decomposition of waveforms for Larsen 500 airborne system. *Geoscience and Remote Sensing, IEEE Transactions On*, *29*(6), 912–921. https://doi.org/10.1109/36.101370

Wong, H., & Antoniou, A. (1994). One-Dimensional Signal-Processing Techniques for Airborne Laser Bathymetry. *IEEE Transactions on Geoscience and Remote Sensing*, *32*(1), 35–46. https://doi.org/10.1109/36.285187